JGR Biogeosciences

RESEARCH ARTICLE
10.1029/2022JG007190

Spectral Induced Polarization (SIP) of Denitrification-Driven Microbial Activity in Column Experiments Packed With Calcareous Aquifer Sediments

C. Strobel[1,2], S. Abramov[1,3], J. A. Huisman[4], O. A. Cirpka[1], and A. Mellage[2]

[1]Department of Geosciences, University of Tübingen, Tübingen, Germany, [2]Civil and Environmental Engineering, University of Kassel, Kassel, Germany, [3]Department of Environmental Microbiology, Institute of Sanitary Engineering, Water Quality and Solid Waste Management, University of Stuttgart, Stuttgart, Germany, [4]Agrosphere (IBG-3), Institute of Bio- and Geosciences, Forschungszentrum Jülich GmbH, Jülich, Germany

Abstract Spectral Induced Polarization (SIP) has been suggested as a non-invasive monitoring proxy for microbial processes. Under natural conditions, however, multiple and often coupled polarization processes co-occur, impeding the interpretation of SIP signals. In this study, we analyze the sensitivity of SIP to microbially-driven reactions under quasi-natural conditions. We conducted flow-through experiments in columns equipped with SIP electrodes and filled with natural calcareous, organic-carbon-rich aquifer sediment, in which heterotrophic denitrification was bio-stimulated. Our results show that, even in the presence of parallel polarization processes in a natural sediment under field-relevant geochemical conditions, SIP is sufficiently sensitive to microbially-driven changes in electrical charge storage. Denitrification yielded an increase in imaginary conductivity of up to 3.1 $\mu S\,cm^{-1}$ (+140%) and the formation of a distinct peak between 1 and 10 Hz, that matched the timing of expected microbial activity predicted by a reactive transport model fitted to solute concentrations. A Cole-Cole decomposition allowed separating the polarization contribution of microbial activity from that of cation exchange, thereby helping to locate microbial hotspots without the need for (bio) geochemical data to constrain the Cole-Cole parameters. Our approach opens new avenues for the application of SIP as a rapid method to monitor a system's reactivity in situ. While in preceding studies the SIP signals of microbial activity in natural sediments were influenced by mineral precipitation/dissolution reactions, the imaginary conductivity changes measured in the biostimulation experiments presented here were dominated by changes in the polarization of the bacterial cells rather than a reaction-induced alteration of the abiotic matrix.

Plain Language Summary To better predict the contribution of microbes to groundwater clean-up it is important to locate microbes in the ground that are actively removing contaminants and measure how fast they are doing so. Our ability to do so, however, is limited by the difficulty in visualizing underground processes. Electrical methods such as spectral induced polarization (SIP) have been applied to monitor microbes and provide an alternative to visualize them underground. SIP, however, has so far only been shown to work in controlled environments and its sensitivity in natural systems remains a question. In this study, we conducted experiments with sediment collected from an underground aquifer, in which we stimulated microbial activity through the addition of nitrate, a widespread groundwater contaminant. Our results show that microbial consumption of nitrate causes a distinct SIP signal that is similar to SIP signals of bacteria in previously studied well-controlled systems. Furthermore, we propose an approach to separate the SIP signal of microbes from that of other processes that occur in natural groundwater. This enables us to quickly asses where the microbes are active and can potentially improve future experiments through the localization of microbial hot-spots and SIP-guided sampling for more detailed microbiological analysis.

Key Points:

- Microbial denitrification in natural sediments can be tracked using spectral induced polarization (SIP)
- σ'' spectra of a natural microbial community match reported spectra from single strains and the level of microbial activity affects σ''
- Superimposing Cole-Cole terms provides a framework for separating microbial and abiotic contributions from SIP signals

Supporting Information:

Supporting Information may be found in the online version of this article.

Correspondence to:

C. Strobel and A. Mellage,
cora.strobel@uni-tuebingen.de;
adrian.mellage@uni-kassel.de

Citation:

Strobel, C., Abramov, S., Huisman, J. A., Cirpka, O. A., & Mellage, A. (2023). Spectral induced polarization (SIP) of denitrification-driven microbial activity in column experiments packed with calcareous aquifer sediments. *Journal of Geophysical Research: Biogeosciences*, *128*, e2022JG007190. https://doi.org/10.1029/2022JG007190

Received 16 SEP 2022
Accepted 28 DEC 2022

Author Contributions:

Conceptualization: C. Strobel, J. A. Huisman, O. A. Cirpka, A. Mellage
Formal analysis: C. Strobel
Funding acquisition: A. Mellage
Investigation: C. Strobel, S. Abramov
Methodology: C. Strobel, S. Abramov, A. Mellage
Project Administration: A. Mellage
Resources: O. A. Cirpka
Software: C. Strobel, A. Mellage
Supervision: J. A. Huisman, O. A. Cirpka, A. Mellage

1. Introduction

Microbially mediated reactions facilitate the in situ degradation of many contaminants in groundwater thus contributing substantially to the water-purification capabilities of the subsurface (Griebler & Avramov, 2015). The ability to understand and predict contaminant removal through microbially mediated reactions in aquifers hinges on our ability to monitor and quantify reaction rates (Pinay et al., 2015) and microbial activity in the subsurface (Leckie et al., 2004). Microbially mediated reactions are subject to spatial variability and temporal dynamics (Li et al., 2021). In general, that spatial variability depends on the co-occurrence of reactants and

Visualization: C. Strobel
Writing – original draft: C. Strobel
Writing – review & editing: C. Strobel, S. Abramov, J. A. Huisman, O. A. Cirpka, A. Mellage

microorganisms, the physicochemical conditions (e.g., temperature and pH), a sufficiently long contact time, and the absence of inhibitors or biotoxins. Direct, non-destructive observations of these parameters over different scales are not possible. Instead, information must be inferred from expensive point measurements, for example, breakthrough curves of solute concentrations at single observation points, or destructive methods (drillings, core extraction), both in field surveys and in laboratory experiments (Werth et al., 2010). Traditional methods for the quantification of microbial abundance, activity and community composition have to rely on destructively-sampled sediment because 80% to >99.9% of the bacteria in groundwater are located at the surfaces of the solid matrix rather than in the mobile water phase (Griebler & Lueders, 2009; Mellage et al., 2015). This is a severe limitation in bench-scale experiments in which sacrificial sampling based on preliminary knowledge can, but not necessarily will capture reaction dynamics (Störiko et al., 2022). Thus, finding easy-to-measure proxies for microbial activity is key for improved monitoring of microbially mediated reactions in porous media.

The reaction of interest of this study is denitrification, that is, the microbial reduction of nitrate (NO_3^-) via several intermediates to N_2, typically coupled to the oxidation of organic carbon, or inorganic electron donors such as Fe(II) or reduced sulfur compounds (Rivett et al., 2008). Excess nitrate, mostly stemming from agriculture, is ubiquitous in aquifers worldwide (Abascal et al., 2022). In oxic environments, NO_3^- is persistent and poses a potential risk to human health when present in sufficiently high concentrations (>10 mg NO_3^--N L^{-1}) in drinking water (Camargo & Alonso, 2006). Denitrification requires the presence of a suitable electron donor, denitrifying bacteria, the absence of oxygen (Kuypers et al., 2018), and sufficiently low flow velocities (Oldham et al., 2013). We chose denitrification and its associated microbial activity, in part, due to their environmental relevance and the challenges that are associated with the quantification of denitrification rates and their monitoring in the field.

Direct measurements of in situ denitrification rates are not only difficult and time consuming (Pinay et al., 2015), their relevance at the larger aquifer-scale is limited by the high spatio-temporal variability of reactive transport in aquifers (Groffman et al., 2006). Gierczak et al. (2007) and Critchley et al. (2014) demonstrated the strong dependence of stimulated in situ denitrification at field sites on the local flow conditions and the microbial response to the addition of an electron donor. Critchley et al. (2014) observed a conditioning phase in which the electron donor, acetate, was injected without any visible effect on NO_3^--concentrations. The conditioning phase was of variable duration at different depths and at different monitoring wells, demonstrating the need to monitor the microbial response in real time and at high spatial resolution.

Non-invasive (bio)geophysical methods offer a promising monitoring alternative that can provide high-resolution information necessary to locate reactive zones in situ and capture reaction dynamics over time (Atekwana & Slater, 2009). Spectral induced polarization (SIP), in particular, has been shown to be sensitive to reactive transport processes, the abundance of bacteria and their metabolic activity in groundwater (see Atekwana & Slater, 2009; Kessouri et al., 2019 for a review). Among the other geophysical methods that have been used for reaction monitoring are seismics and direct-current (DC) geoelectrics (Che-Alota et al., 2009; Williams et al., 2005). The latter methods, however, do not depend on microbial activity itself but on its impact on the physical properties of the matrix or pore fluid, for example, mineral precipitation-driven changes in sediment stiffness (e.g., Saneiyan et al., 2020). Thus, limiting the applicability and transferability of such methods to other sites or reaction types. Conversely, the measurement principle of SIP is directly sensitive to the electrochemical properties of microbes (Kessouri et al., 2019) and could, in theory, be applied to any microbially-mediated reaction system.

In SIP, an alternating current at different frequencies in the mHz to kHz range is injected into the subsurface via an electrode pair, and the voltage is measured by a second pair (Marshall & Madden, 1959). The resulting impedance Z (Ω) and phase shift $-\Phi$ (rad) are typically expressed in the complex-valued phase notation. The corresponding material property, the conductivity σ^* (S m^{-1}), is also complex-valued. Its magnitude depends on electrical conduction through the pore fluid and along charged surfaces as well as on reversible electrical storage at charged surfaces (e.g., Binley & Slater, 2020 and references therein). In the applied frequency range, the real (in-phase) component σ' (S m^{-1}) is hardly affected by the small phase shifts in the mrad-range. It is almost identical to the DC conductivity, σ_0 (S m^{-1}), and mainly depends on the electrical conductance, σ_{el} (S m^{-1}), of the pore fluid through connected pores and, to a smaller extent, on electrical conduction along the grain-fluid interface, σ_{surf} (Slater & Glaser, 2003). The imaginary (out-of-phase or quadrature) conductivity, σ'' (S m^{-1}), is much smaller than σ'. It is approximately proportional to the product of the phase shift Φ and the DC conductivity and exhibits a strong frequency-dependence. Phenomenological models, such as the Cole-Cole relaxation model (Cole & Cole, 1941; Pelton et al., 1978), are commonly employed to help summarize the frequency dependent

polarization behavior of SIP measurements via a few characteristic parameters. Such models can be particularly helpful to analyze spectral data sets over time as they enable the quantification of changes in spectral shape and peak frequency alongside changes in the magnitude of polarization (Mellage, Smeaton, et al., 2018; Ntarlagiannis et al., 2010).

In porous media, in the absence of metallic particles and in the low-frequency range (mHz to kHz), charge storage is mainly controlled by electrochemical polarization of the electrical double layer (EDL) that surrounds the charged surfaces of minerals and colloids. Both the polarization of the EDL of single particles, mainly in the Stern layer (Leroy et al., 2008; Lesmes & Morgan, 2001; Schwarz, 1962) and membrane polarization, caused by a difference in the mobility of anions and cations at pore throats, contribute to charge storage (Marshall & Madden, 1959; Revil & Florsch, 2010; Titov et al., 2002). Several modeling approaches have been successful at predicting the spectral responses of glass beads and clay minerals by accounting for Stern layer polarization only (e.g., Jougnot et al., 2010; Leroy & Revil, 2009; Leroy et al., 2008). The properties of the EDL directly influence the magnitude and spectral dependency of σ'' responses. A higher surface charge leads to a higher concentration of counter ions within the EDL, yielding higher σ'' signals (Hao et al., 2015). The peak frequency is dependent on the length scale of polarization, that is, the particle size or pore size (e.g., Scott & Barker, 2003; Titov et al., 2002; Weller & Slater, 2019), and the mobility of the counter ions in the EDL (Schwarz, 1962). In porous media saturated with solutions containing more than two ions, the replacement of monovalent cations by divalent cations is known to reduce the magnitude of charge storage, due to their difference in surface mobility (Ben Moshe et al., 2021). Consequently, σ'' depends on both the ionic composition of the pore fluid and the surface properties of the matrix.

The polarization of microbes is to some extent similar to electrochemical polarization on mineral surfaces. Their cell-membrane surface contains charged functional groups that yield a net-negatively charged surface in the near neutral pH range (Poortinga et al., 2002). Moreover, the cell membrane acts as an electrical insulator between the cell interior and bulk solution (van der Wal et al., 1997). Thus, microbes can be conceptualized as additional particles that contribute to the overall complex-conductivity response of a porous medium (Kessouri et al., 2019; Mellage et al., 2019; Revil et al., 2012; Sanchis et al., 2007).

In biogeophysical studies, σ'' responses have been linked to microbial abundance and growth, not only in cell suspensions (Rosier et al., 2019; Zhang et al., 2014), but also in porous matrices that exhibit a low background polarization, such as glass beads and quartz sand (Abdel Aal et al., 2010; Davis et al., 2006; Mellage, Smeaton, et al., 2018). SIP has been successfully used to study nitrate reduction in sands (Mellage, Holmes, et al., 2018; Mellage et al., 2019), hydrocarbon degradation (Abdel Aal et al., 2004, 2006; Kimak et al., 2019), bacterial growth in a saline environment (Joo et al., 2021) and microbially induced precipitation of calcite (Saneiyan et al., 2019) and sulfide (Ntarlagiannis et al., 2005; Williams et al., 2005) at the laboratory scale, highlighting the potential of SIP to serve as a monitoring tool for a variety of microbially mediated processes. The method has also gained increasing interest in the live-monitoring of bioreactors (Turick et al., 2019). Electrical impedance spectroscopy (EIS), a 2-point measurement technique similar to SIP, is used by bioelectrochemists, where "low-frequency EIS" refers to the same frequency range that is traditionally used in biogeophysics. Slouka et al. (2016) refer to their 4-point measurements of microbial growth also as low frequency EIS but the measurement set-up is very similar to SIP measurements. Reported peak frequencies or fitted Cole-Cole peak frequencies that are related to the presence of bacteria range from 0.1 to 1 Hz (Joo et al., 2021; Zhang et al., 2014) to 2–30 Hz (Mellage, Holmes, et al., 2018; Mellage et al., 2019; Rosier et al., 2019; Zhang et al., 2014). In other studies, spectra were not presented or not acquired. Instead, complex conductivity was monitored at a specific frequency, typically 1 Hz (Katona et al., 2021) or 10 Hz (Abdel Aal et al., 2010).

Despite growing evidence that SIP signals are affected by microbial abundance and activity, the unique attribution of SIP signals to microbial processes in natural sediments has not been investigated and might be more difficult to capture than in packings of glass beads or clean quartz sand. Hence, we see the need for experiments of increased complexity, yet under controlled laboratory conditions, to investigate the sensitivity of SIP toward microbial reactions and to develop quantitative relationships between microbial abundance or activity and σ'' in the presence of other processes that contribute to SIP signals. The aim of the present study is to answer the following questions: (a) Do microbial reactions yield a measurable SIP signal under close-to-natural conditions? (b) What is the σ'' spectrum of a natural microbial community? and (c) What information is required to separate the microbial σ'' signals from parallel abiotic polarization processes? To this end, we stimulated microbial denitrification in an organic-carbon-rich calcareous sediment with its indigenous microbial community by injecting nitrate into

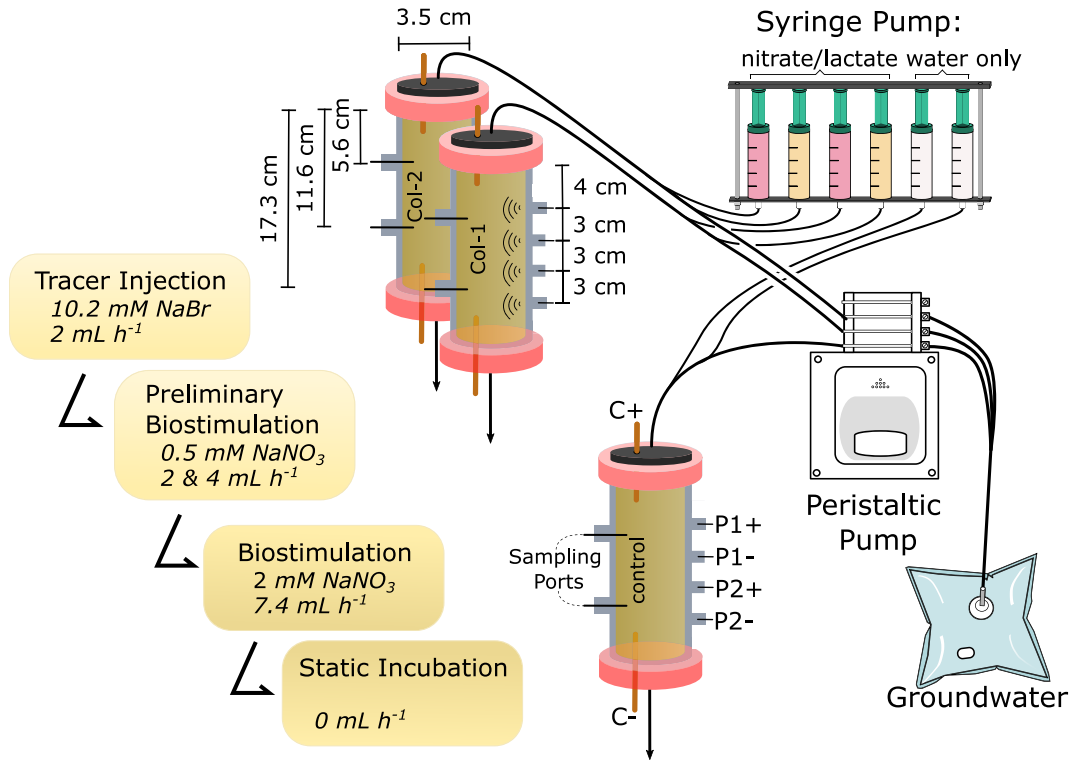

Figure 1. Experimental setup: The columns were equipped with four potential electrodes along the flow path and two current electrodes at the top and bottom caps. Two pore water sampling ports were located at 5.6 and 11.6 cm from the inlet. The inflowing solution consisted of natural anoxic groundwater, to which the tracer salts were added directly before the inlet using a syringe pump.

flow-through columns. Therein, we obtained breakthrough curves of reactants and synchronously measured changes in the σ'' spectrum. We jointly interpret these data to link the dynamic, denitrification-driven activity of the natural microbial community to the measured σ'' signals. To separate the effects of microbial activity and abiotic ion-exchange reactions we also performed experiments in which we injected a NaBr pulse. We propose a Cole-Cole decomposition (using two terms) in which one set of parameters relates to the abiotic contribution of the bulk polarization response, and the other set of parameters to the microbial contribution. Furthermore, we fitted a reactive transport model to the concentration time series of both the NaBr- and NO_3^--injection phases to quantitatively relate SIP signals to ion exchange reactions and denitrifying microbial activity.

2. Materials and Methods

2.1. Setup of Flow-Through Columns

The flow-through experiment was conducted in four phases of different inflow conditions in three columns, out of which two served as biostimulated duplicates, Col-1 and Col-2, and one served as the non-biostimulated control. Figure 1 shows the experimental flow-through set-up with three glass columns ($L = 17.3$ cm, $d = 3.5$ cm) and an inflow system made up of a peristaltic pump that provided groundwater and a syringe pump for the addition of reactants, that is, sodium bromide (NaBr), sodium nitrate ($NaNO_3$) or sodium lactate (NaLac). The ratio of groundwater to reactant-containing solution was 10:1 (*v/v*). Each column was fitted with brass electrodes ($d = 0.5$ cm) at the column inlet and outlet for current injection, and four brass potential electrodes ($d = 0.5$ cm) 4, 7, 10, and 13 cm from the inlet. The potential electrodes were retracted from the current flow path and encased in an agar gel electrolyte. Additionally, each column was equipped with ceramic samplers at 5.6 and 11.6 cm from the inlet that facilitated the sampling of pore water at the midpoint of the potential electrode pairs. The columns were wet packed at ambient air with homogenized sediment from a depth of 2.4–7.4 m of the Ammer floodplain aquifer, near Tübingen, Germany, henceforth referred to as the Tufa aquifer (Klingler et al., 2020; Martin et al., 2020). The sediment, a poorly consolidated tufa, is a mixture of biogenous carbonate precipitates (~85%)

and organic matter, with an average total organic carbon (TOC) content of 5.7% for the homogenized sediment. Groundwater from the anoxic region of the Ammer aquifer was directly pumped into air-tight bags (Tedlar®, Sigma Aldrich) and used as the inflowing solution, thereby mimicking natural conditions. For further details on the packing procedure and a photograph of the columns see the section Text S1 and Figure S1a in Supporting Information S1.

The experiment was conducted in a temperature-controlled chamber at 12°C, the mean groundwater temperature of the Tufa aquifer. Initially, the columns were allowed to equilibrate with the groundwater for 7 days via a continuous injection at a flow rate of 2 mL hr^{-1}. During the last 100 hr of the equilibration phase, SIP measurements were performed (Figure S2 in Supporting Information S1). Following the equilibration phase, a 10.2 mM NaBr tracer solution was injected over 48 hr at a pumping rate of 2.00 ± 0.16 mL hr^{-1} (flow velocity, v: 5 cm d^{-1}), to capture the conservative transport of Br^- and thereby estimate physical transport parameters. Concentration samples were periodically collected at the outflow (Na^+, Br^- and major ions) of Col-1, in addition to concurrent SIP measurements at all three columns, over 192 hr (8 days).

The tracer injection was followed by a preliminary biostimulation phase in which $NaNO_3$ (0.5 mmol L^{-1}) and NaLac (0.5 mmol L^{-1}) were injected continuously at varying flow rates. During biostimulation, two columns (Col-1 and Col-2) received the biostimulating solutions whereas the third column served as a control and received unaltered groundwater stock plus ultra-pure water (MilliQ®, Millipore, USA) from the syringe pump. Lactate was added as a primer to enhance and accelerate denitrification and shorten potential lag times of microbial activity (Blagodatskaya & Kuzyakov, 2008). During the preliminary biostimulation phase, the flow rate and nitrate inflow concentration were adjusted until nitrate was detected in outflow samples. This was followed by the main biostimulation phase (henceforth referred to as the biostimulation phase) with an average flow rate and NO_3^--concentration of 7.2 mL hr^{-1} (v: 0.16 m d^{-1}) and 4.0 mmol L^{-1} over 162 hr (6.75 days), respectively and a lactate concentration of 0.5 mmol L^{-1}. Pore water and outflow samples were collected daily, and SIP measurements were performed every 4 hr. For each sampling event, initially 0.5 mL of pore water were extracted and discarded (dead volume of the sampler), followed by the extraction of 1 mL of sample. Finally, flow was stopped, and the columns were incubated for 840 hr (35 days) under no-flow conditions, yielding a final static phase. During the static phase, pore water samples were taken at a weekly interval to monitor the extent of nitrate reduction, and SIP measurements continued at a 4–8 hr interval. During pore water sampling, the columns were connected to an air-tight groundwater reservoir bag (Tedlar®, Sigma Aldrich) at the inflow and outflow, enabling inflow of groundwater to replace the sampled volume, thus maintaining constant water saturation during the entire phase.

We decided to forfeit direct cell counting and DNA quantification via sacrificial sampling of the sediment because it would have required a prohibitive number of replicates for adequate monitoring of temporal dynamics. Moreover, while preliminary experiments had shown that microbial cells could be successfully detached from the Tufa sediment, reliable cell counting was impeded by the high background fluorescence of the organic matter present in the sediment (see Text S3 and Figure S4 in Supporting Information S1). Therefore, we relied on a DNA quantification during a preliminary nitrate reduction experiment to confirm the presence of denitrification functional genes and the microbial community's capacity to reduce NO_3^- (Text S2 and Figure S3 in Supporting Information S1).

2.2. Geochemical Analysis of Pore Water and Outflow Samples

Geochemical analyses of the pore water were conducted on samples collected at the outflow and at both sampling ports (5.6 and 11.6 cm). Prior to analysis, the samples were filtered (0.45 µm), diluted if necessary and stored at 4°C. Major ions were quantified with an ion chromatograph (Metrohm, Germany). Bicarbonate concentrations were estimated by closing the ion balance of major ions. NO_3^--, NO_2^--and NH_4^+-concentrations were quantified colorimetrically using a continuous-flow analyzer (Seal Analytical Norderstedt, Germany) and lactate concentrations were quantified via high-performance liquid chromatography (HPLC) (Shimadzu Deutschland GmbH, Germany).

2.3. SIP Measurements

SIP spectra were recorded at regular intervals using a measurement script (Störiko, 2019) that enabled automation of time series measurements using the Portable SIP Unit (Ontash and Ermac Inc., U.S.). Phase shift ($-\Phi$) and

impedance magnitude ($|Z|$) were measured over 51 log-frequency intervals between 0.01 and 1,000 Hz with a reference resistor of 1,000 Ω and an amplitude of 5 V. The results were converted to apparent, spatially uniform, frequency-dependent complex conductivities via the geometric factor of the given electrode setup. The geometric factor of the electrode set-up was determined experimentally through measurements of the apparent electrical conductivity of the columns filled with water of known conductivity.

2.4. Reactive Transport Modeling

We simulated reactive transport of the solutes through the column via the one-dimensional (1-D) advection-dispersion-reaction equation, accounting for the mass balance of both aqueous and sorbed concentrations for solutes that undergo cation exchange:

$$\frac{\partial C}{\partial t} + \frac{(1-n_e)\rho_s}{n_e}\frac{\partial S}{\partial t} + v\frac{\partial C}{\partial x} - D\frac{\partial^2 C}{\partial x^2} = R \tag{1}$$

in which C (mmol L^{-1}) and S (mmol g^{-1}) are the aqueous- and solid-phase concentrations for a sorbing compound, respectively, t and x denote the temporal and spatial coordinates, R (mmol L^{-1} h^{-1}) is the net reaction rate of all microbial transformations, n_e (−) is the effective porosity of the Tufa pack, ρ_s (g L^{-1}) is the mass density of the solids (approximated herein as that of quartz, 2,650 g L^{-1}, which is in the range of values reported for calcite), v (m s^{-1}) is the effective linear velocity, and D (m^2 s^{-1}) is the dispersion coefficient, calculated from the pore diffusion coefficient (D_p in m^2 s^{-1}) of each compound and the Tufa-specific dispersivity (α in m), using the approach of Scheidegger (1961): $D = \alpha v + D_p$. Equation 1 is subject to a known flux-boundary condition at the inlet and a zero-dispersive flux boundary condition at the outlet. For solutes that do not undergo cation exchange (i.e., anions) the second term in Equation 1 drops out. An overview of all model parameters and the system of governing equations is provided in Text S4 and Tables S2 and S3 in Supporting Information S1.

The ion exchange between Na^+ and major cations (Ca^{2+} and Mg^{2+}) was simulated via competitive sorption, where reversible sorption rates, r^{Na}_{sorb} and r^{Me}_{sorb}, in mmol of charge ($mmol_c$) g^{-1} s^{-1}, for Na^+ and Me^{2+} (the sum of Ca^{2+} and Mg^{2+}), respectively, were driven by the difference between equilibrium, $S^{eq}_{Na/Me}$, and actual, $S_{Na/Me}$, concentrations of sorbed cations ($mmol_c$ g^{-1}). The equilibrium concentrations were computed by solving for the aqueous and sorbed concentrations for a given total amount of solute via a fixed-point (Picard) iteration assuming the following generalized Langmuir isotherm, shown here for the competitive sorption of Na^+ and the sum of divalent cations (Me^{2+}):

$$S^{eq}_{Na} = \frac{s_{max}\cdot C_{Na}}{C_{Na} + K^{Na}_{ads}\left(1 + \frac{C_{Me}}{K^{Me}_{ads}}\right)} \tag{2}$$

$$r^{Na}_{sorb} = \lambda\left(S^{eq}_{Na} - S_{Na}\right) \tag{3}$$

$$r^{Me}_{sorb} = \lambda\left(S^{eq}_{Me} - S_{Me}\right) \tag{4}$$

in which, C_{Na} and C_{Me} ($mmol_c$ L^{-1}) are the aqueous phase concentrations of Na^+ and Me^{2+}, respectively, s_{max} ($mmol_c$ g^{-1}) is the maximum sorption capacity of the Tufa sediment, and K^{Na}_{ads} and K^{Me}_{ads} ($mmol_c$ L^{-1}) are the binding constants of Na^+ and Me^{2+}, respectively, and λ (s^{-1}) is the kinetic mass-transfer rate constant. An identical formulation for S^{eq}_{Me} can be obtained by replacing "Na" terms by "Me" terms and using $r^{Me}_{sorb} = -r^{Na}_{sorb}$.

Denitrification coupled to the oxidation of both lactate and organic carbon derived from the solid matrix was simulated using Monod kinetics and explicitly considering the biomass of the denitrifying microbial community as an immobile species. We considered a constant cell density and accounted for microbial activation and deactivation in the presence or absence of NO_3^-, via the switch-function approach of Stolpovsky et al. (2011) and Mellage et al. (2015). In natural sediments cell densities are relatively stable, but facets of the microbial community are known to become active in response to the presence or absence of substrates (Lennon & Jones, 2011). Thus, by simulating activation and deactivation our model formulation enables the prediction of active biomass. Denitrification was simulated as a two-step reaction where each electron donor was coupled to the reduction of

nitrate to nitrite and nitrite to N_2. The rates of denitrification $r_{\mathrm{lac}}^{\mathrm{DNO}_x}$ (mmol L^{-1} s^{-1}) for the two successive steps are:

$$r_{\mathrm{lac}}^{\mathrm{DNO}_x} = \frac{\mu_{\mathrm{max}}^{\mathrm{NO}_x}}{Y_{\mathrm{lac}}} \left(\frac{C_{\mathrm{Lac}}}{C_{\mathrm{Lac}} + K_{\mathrm{Lac}}} \right) \left(\frac{C_{\mathrm{NO}_x}}{C_{\mathrm{NO}_x} + K_{\mathrm{NO}_x}} \right) \frac{(1 - n_{\mathrm{e}})\rho_{\mathrm{s}}}{n_{\mathrm{e}}} \mathrm{BIO}_{\mathrm{act}} \tag{5}$$

in which $\mu_{\mathrm{max}}^{\mathrm{NO}_x}$ (s^{-1}) is the maximum specific growth rate constant, Y_{lac} (cells mmol-Lac^{-1}) is the microbial yield coefficient, C_{Lac} (mmol L^{-1}) the concentration of lactate, K_{Lac} (mmol L^{-1}) is the lactate half-saturation constant, C_{NO_x} (mmol L^{-1}) and K_{NO_x} (mmol L^{-1}) are the concentration and half-saturation constant of NO_3^- ($x = 3$) or NO_2^- ($x = 2$) and $\mathrm{BIO}_{\mathrm{act}}$ (cells g^{-1}) is cell density of active biomass. To describe the system's response to priming with lactate, we included a release of readily bioavailable dissolved organic carbon (DOC) from the matrix, directly dependent on the concentration of lactate and a first-order hydrolysis rate coefficient, k_{hyd} (s^{-1}):

$$r_{\mathrm{hyd}} = k_{\mathrm{hyd}} C_{\mathrm{Lac}} \tag{6}$$

Here, we assumed that the priming led to an overall increase in microbial activity, thus increasing the hydrolysis of solid organic carbon (SOC) to readily biodegradable DOC that was also available as an electron donor for denitrification. Assuming that the hydrolysis yields a labile DOC that is very bioavailable, the sequential rates of denitrification coupled to DOC oxidation share the same rate coefficients as the lactate-dependent rates:

$$r_{\mathrm{DOC}}^{\mathrm{DNO}_x} = \frac{\mu_{\mathrm{max}}^{\mathrm{NO}_x}}{Y_{\mathrm{lac}}} \left(\frac{C_{\mathrm{DOC}}}{C_{\mathrm{DOC}} + K_{\mathrm{Lac}}} \right) \left(\frac{C_{\mathrm{NO}_x}}{C_{\mathrm{NO}_x} + K_{\mathrm{NO}_x}} \right) \frac{(1 - n_{\mathrm{e}})\rho_{\mathrm{s}}}{n_{\mathrm{e}}} \mathrm{BIO}_{\mathrm{act}} \tag{7}$$

Finally, a lactate-independent denitrification reaction coupled to the oxidation of SOC was implemented. It was formulated as a single Monod rate law due to the high amount of organic carbon in the sediment that was assumed to be non-limiting:

$$r_{\mathrm{SOC}}^{\mathrm{DNO}_x} = \frac{s\mu_{\mathrm{max}}^{\mathrm{NO}_x}}{Y_{\mathrm{SOC}}} \left(\frac{C_{\mathrm{NO}_x}}{C_{\mathrm{NO}_x} + sK_{\mathrm{NO}_x}} \right) \frac{(1 - n_{\mathrm{e}})\rho_{\mathrm{s}}}{n_{\mathrm{e}}} \mathrm{BIO}_{\mathrm{act}} \tag{8}$$

in which $s\mu_{\mathrm{max}}^{\mathrm{NO}_x}$ (s^{-1}) is the maximum specific growth rate constant for denitrification coupled to SOC, sK_{NO_x} (mmol L^{-1}) are the half-saturation constant of NO_3^- ($x = 3$) or NO_2^- ($x = 2$) and Y_{SOC} (cells mmol-SOC^{-1}) is the corresponding microbial yield coefficient.

The activation and deactivation rates of the microbial consortium, r_{act} and r_{deact} (cells g^{-1} s^{-1}), respectively, were modeled using first-order kinetics and scaled via a switch-function, θ (−), that determines the favorability of activation, that is, whether or not electron acceptor (i.e., nitrate) is present:

$$r_{\mathrm{act}} = \theta k_{\mathrm{act}} \mathrm{BIO}_{\mathrm{ina}} \tag{9}$$

$$r_{\mathrm{deac}} = (1 - \theta) k_{\mathrm{act}} \mathrm{BIO}_{\mathrm{act}} \tag{10}$$

$$\theta = \frac{1}{\exp\left(\frac{C_{\mathrm{NO3}}^{\mathrm{thresh}} - C_{\mathrm{NO3}}}{st \cdot C_{\mathrm{NO3}}} \right) + 1} \tag{11}$$

where k_{act} (s^{-1}) is the first-order activation and deactivation rate coefficient and $\mathrm{BIO}_{\mathrm{ina}}$ (cells g^{-1}) is the cell density of inactive biomass. The switch-function in Equation 11 can take on values between 0, maximally unfavorable conditions, and 1 during optimal conditions. The magnitude of θ depends on the difference between C_{NO3} and a pre-defined activation threshold nitrate concentration, $C_{\mathrm{NO3}}^{\mathrm{thresh}}$. The non-dimensional coefficient *st* determines the steepness of the transition between the limits of the switch-function (Stolpovsky et al., 2011).

The model was discretized in space by the finite volume method, converting the reactive transport equations to a nonlinear system of ordinary differential equations which was solved in MATLAB using the ordinary-differential-equation solver, ode15s (Shampine & Reichelt, 1997).

2.5. Cole-Cole Model

The Cole-Cole relaxation model (Pelton et al., 1978) is a phenomenological model that parameterizes the frequency-dependent complex resistivity of SIP measurements exhibiting a single spectral peak:

$$\rho^* = \rho_0 \cdot \left(1 - m \cdot \left(1 - \frac{1}{1 + (i \cdot \omega \cdot \tau)^c}\right)\right) \tag{12}$$

where ρ^* (Ω m) is the modeled complex resistivity (i.e., the inverse conductivity), ρ_0 (Ω m) is the DC resistivity, ω (rad) is the angular frequency, m (−) is the chargeability, τ (s) is a time constant related to the peak frequency, and c (−) is the Cole-Cole exponent that describes the broadness of the polarization peak (Pelton et al., 1978).

We extended the Cole-Cole model to account for two parallel charge-storage contributions stemming either from the sediment matrix or from the active microbial community:

$$\rho^* = \rho_0 \cdot \left(1 - \left(m_{\text{mat}} \cdot \left(1 - \frac{1}{1 + (i \cdot \omega \cdot \tau_{\text{mat}})^{c_{\text{mat}}}}\right) + m_{\text{bac}} \cdot \left(1 - \frac{1}{1 + (i \cdot \omega \cdot \tau_{\text{bac}})^{c_{\text{bac}}}}\right)\right)\right) \tag{13}$$

in which all terms have the same meaning as in the single Cole-Cole model but the subscripts "mat" and "bac" refer to the matrix- and bacterial-specific coefficients. In the following we refer to the matrix-related contribution to polarization as $\text{CC}_{\text{matrix}}$ (CC = Cole-Cole) and to the polarization induced by the microbial community as $\text{CC}_{\text{bacteria}}$. The log-transformed parameter values were fitted to the measured spectral responses using the trust-region-reflective algorithm (Coleman & Li, 1996) via the function lsqnonlin in Matlab. We constrained the parameter ranges based on the following reasoning. First, we assumed that the parameters defining the spectral shape of the matrix-polarization contribution, τ_{mat} and c_{mat}, should not deviate more than 5% from the mean parameters $\overline{\tau}_0$ and $\overline{c}_0$ of single Cole-Cole fits to the first five spectra measured after the start of the experiment before the NaBr injection. Second, we assumed that the characteristic peak frequency associated with the polarization of bacteria should resemble that of previously reported spectra for bacteria, with a distinct peak around 2–30 Hz (Mellage, Holmes, et al., 2018; Mellage et al., 2019; Rosier et al., 2019; Zhang et al., 2014). Hence, a Cole-Cole exponent c_{bac} greater than 0.5, limiting the broadness of the peak, and a time constant τ_{bac} between 1.13×10^{-2} and 1 s were chosen as constraints for the bacterial term. As an initial guess for all matrix parameters, we used the mean parameters $\overline{\rho}_0$, $\overline{m}_0$, $\overline{\tau}_0$ and $\overline{c}_0$ of a single Cole-Cole fit to the first five spectra after the start of the experiment and before the NaBr injection.

3. Results and Discussion

In the following, we present and discuss the results of both the tracer (NaBr) injection and the biostimulation experiment. For conciseness, we focus our discussion of the biostimulation phase (NO_3^--injection) on the data collected in Col-1. Wherever possible, without limiting the readability of the figures, the results of the replicate (Col-2) and control column are shown as well. Otherwise, those data are presented in the Supporting Information S1.

3.1. Conservative Tracer Injection

3.1.1. Solute Concentrations

Figure 2 compares breakthrough curves of Br^- and major cations (Na^+, Ca^{2+}, and Mg^{2+}) at the column outlet (17.3 cm) and time series of the change of the maximum σ' and σ'', relative to pre-injection values during the NaBr-injection phase, to the results of the reactive transport model. The measured outlet concentrations of Br^- (maximum of 9.6 mmol L^{-1}) agree well with the expected behavior of a conservative compound undergoing advective-dispersive transport (Figure 2a). The fit of the model yields an effective porosity (n_e) of 76% and a dispersivity (α) of 0.4 mm for the homogenized Tufa pack. The high porosity reflects the high content of organic matter (peat) in the sediment (Rezanezhad et al., 2017) and agrees with the Tufa's aquatic sediment-like consistency and microporous structure of the Tufa particles (see Figure S1b in Supporting Information S1).

Relative to Br^-, the arrival of its counter ion Na^+ at the outlet was retarded by approximately 10 hr, with a lower peak concentration of 6.2 mmol L^{-1}. The peak arrival of Na^+ occurred 26.5 hr after the arrival of a pulse of Ca^{2+}

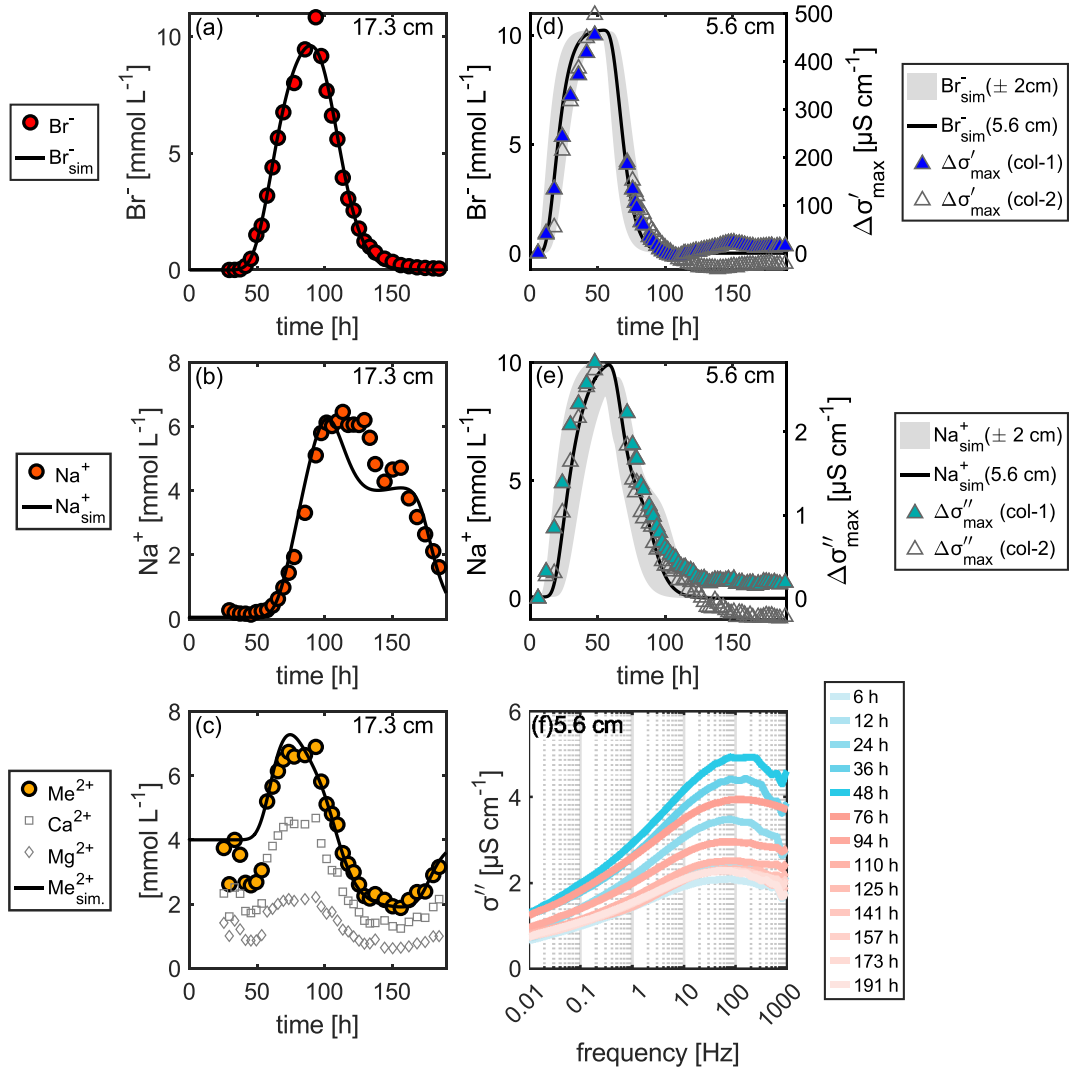

Figure 2. Measured and simulated breakthrough curves at the column outlet, $l = 17.3$ cm, and at the location of the first potential electrode pair ($l = 5.6$ cm); (a, d) Br^-; (b, e) Na^+; (c) Me^{2+} ($Ca^{2+} + Mg^{2+}$). The simulated aqueous Br^- and Na^+ concentrations at $l = 5.6$ cm are compared to the measured change (Δ) in σ'_{max} and σ''_{max} in panels (d) and (e). The shaded areas depict the concentration breakthrough at 5.6 $\pm$ 2 cm. Time-lapse changes in σ'' spectra at location 5.6 cm in Col-1 are shown in (f).

and Mg^{2+}. Because both Ca^{2+} and Mg^{2+} responded equally to the tracer injection and remained at a relatively constant 2:1 ratio, they are presented and discussed here as their sum, Me^{2+} (Figure 2c). The competitive sorption model was able to accurately capture the timing and extent of Na^+ and Me^{2+} breakthrough. The measured peak Na^+ concentration remained constant for about 30 hr (between 97 and 130 hr) followed by a concentration drop, driven by the shift to NaBr-free solution at the inlet (at 48 hr). The concentration drop exhibited a small shoulder from 137 to 156 hr at 4.7 mmol L^{-1} and a longer tailing than Br^- (Figure 2b). The model predicts a more rapid decrease in concentration after the peak concentration is reached and a more pronounced shoulder from 129 to 161 hr at 4.1 mmol L^{-1} (Figure 2b). We attribute the discrepancy to slight differences in the cation exchange between Ca^{2+}–Na^+ and Mg^{2+}–Na^+ that were neglected in our model formulation.

Concentrations of Ca^{2+} and Mg^{2+} increased due to cation exchange-driven release (Amrhein & Suarez, 1990; Poonia & Talibudeen, 1977; Rahman & Rowell, 1979) in the presence of Na^+, followed by a concentration drop to about half of the inflow concentration during the reverse reaction as NaBr-free solution was injected. The initial Ca^{2+} and Mg^{2+} concentrations were approached by the end of the tracer injection (Figure 2c) as the remaining Na^+ was released and Ca^{2+} and Mg^{2+} became the dominant species. The ability of the competitive sorption model

to capture the dynamics in cation concentrations confirms that cation exchange, driven by the incoming high Na^+ concentration, caused the replacement of divalent cations by Na^+ in the mineral and organic matter EDLs. The process was reversed once NaBr-free groundwater replaced the tracer solution at the inlet.

3.1.2. SIP Response

The dynamics in the geochemical composition of the pore fluid and surface sites were associated with σ' and σ'' changes. The breakthrough of Br^- caused an increase in the DC electrical conductivity of the pore fluid, and consequently in σ' at the first potential electrode pair ($l = 5.6$ cm), see Figure 2d (for $l = 11.6$ cm, see Figure S5 in Supporting Information S1). The simulated peak concentration of 9.9 mmol L^{-1} at 5.6 cm coincides with an increase in σ' of 455 and 497 µS cm^{-1} from a starting value, $\sigma'(t_0)$, of 380 and 440 µS cm^{-1} in Col-1 and Col-2, respectively. After 100 hr, the pre-injection level was approached, with σ' stabilizing at 393 µS cm^{-1} in Col-1 and 420 µS cm^{-1} in Col-2. In general, both columns showed consistent σ' dynamics that agree well with the simulated breakthrough of Br^--ions, the ion that dominated the changes in pore water conductivity. Potential electrode pairs measure integrated SIP signals over an electrode response volume, determined by the geometry of the setup (Mellage, Holmes, et al., 2018). Thus, while the major contribution is expected to stem from the midpoint of the electrodes, measurements inherently contain contributions from a spatial interval. Hence, we compare SIP measurements to breakthrough concentrations at the midpoint of the electrodes and at the midpoint ± 2 cm. The range is shown as the shaded gray area in Figures 2d and 2e.

We observed an increase in the maximum σ'' of up to 2.8 µS cm^{-1} as Na^+ arrived at 5.6 cm (Figure 2e). Similarly, the tailing of σ'' matched the simulated drop in aqueous Na^+ concentration. The temporal changes of simulated aqueous Na^+ concentrations and σ'' coincide and are consistent between Col-1 and Col-2. The increase in σ'' is driven by the higher surface mobility of Na^+ in the EDL relative to Ca^{2+} and Mg^{2+} (Ben Moshe et al., 2021). Analogous to the σ', σ'' approached pre-injection levels after the NaBr injection, leveling off at 2.27 and 2.67 µS cm^{-1} in Col-1 and Col-2, respectively. A carbonate dominated system like the Tufa is susceptible to precipitation-dissolution processes that can be induced by several factors, for example, changing cation or bicarbonate concentrations and subtle pH changes (Morse et al., 2007; Tamir et al., 2012) that can influence the pore-fluid and EDL composition and thus SIP signals. The experimental setup herein was designed to minimize these secondary contributions (e.g., by using groundwater from the same site as the sediment and storing the collected groundwater in gas-tight bags to maintain the CO_2 partial pressure) and it is thus beyond the scope of this work to quantify them. The excellent agreement of the competitive sorption model with the cation breakthrough suggests that carbonate dissolution played only a minor role. However, it may explain the small differences in the SIP signals before and after tracer injection.

Despite the considerable changes in σ'', the cation exchange process did not exhibit a strong influence on the spectral shape of σ''. In Figure 2f, σ'' spectra are shown for different time-points during the tracer injection in Col-1 at 5.6 cm from the inlet (spectra of the other columns and at 11.6 cm are shown in Figures S7b, S7c, S8b, and S8c in Supporting Information S1). The sediment has a background polarization between 0.7 and 2 µS cm^{-1}. It increases steadily toward higher frequencies, reaching a broad peak at around 50–400 Hz, and decreases toward 1,000 Hz. During the NaBr injection, variations in σ'' exhibited the same general trend at all frequencies. There was no development of a clear peak nor a shift in peak frequency. At the end of the NaBr-injection, σ'' spectra approached the pre-injection magnitude, highlighting the reversibility of the cation-exchange process. The phase shift of the Tufa ranged between 1.7, at low frequencies, and 6.2 mrad at peak frequencies and reached up to 8.7 mrad during the NaBr injection (Figures S9, and S10a–S10c in Supporting Information S1).

In silica- and mineral dominated-porous media, that is, devoid of organic matter, Vaudelet et al. (2011), Hao et al. (2015) and Mellage et al. (2022) showed that changes in surface-associated ion concentrations are proportional to σ''-changes. In contrast, the σ''-dynamics, herein, did not entirely reflect changes in sorbed Na^+ concentrations (Figure S6b in Supporting Information S1), but rather more closely traced the presence of Na^+ in the aqueous phase (Figure 2e). In organic-matter-containing soils, as is the case for the Tufa sediment, Mellage et al. (2022) showed that while σ'' does change in response to sorption, changes are not proportional to sorbed concentrations (therein, of a divalent organic cation). We speculate, that in a more complex organic-matter-containing matrix, like the Tufa, poorly-understood polarization mechanisms in the organic matter (Katona et al., 2021; Mellage et al., 2022), drive the observed discrepancy. Thus, suggesting that the relationship between σ'' and counter ions in the EDL, under temporally variant geochemical conditions, may in fact be more complex than previously thought, especially in natural sediments with different types of sorption sites/polarizable media. Nevertheless, our

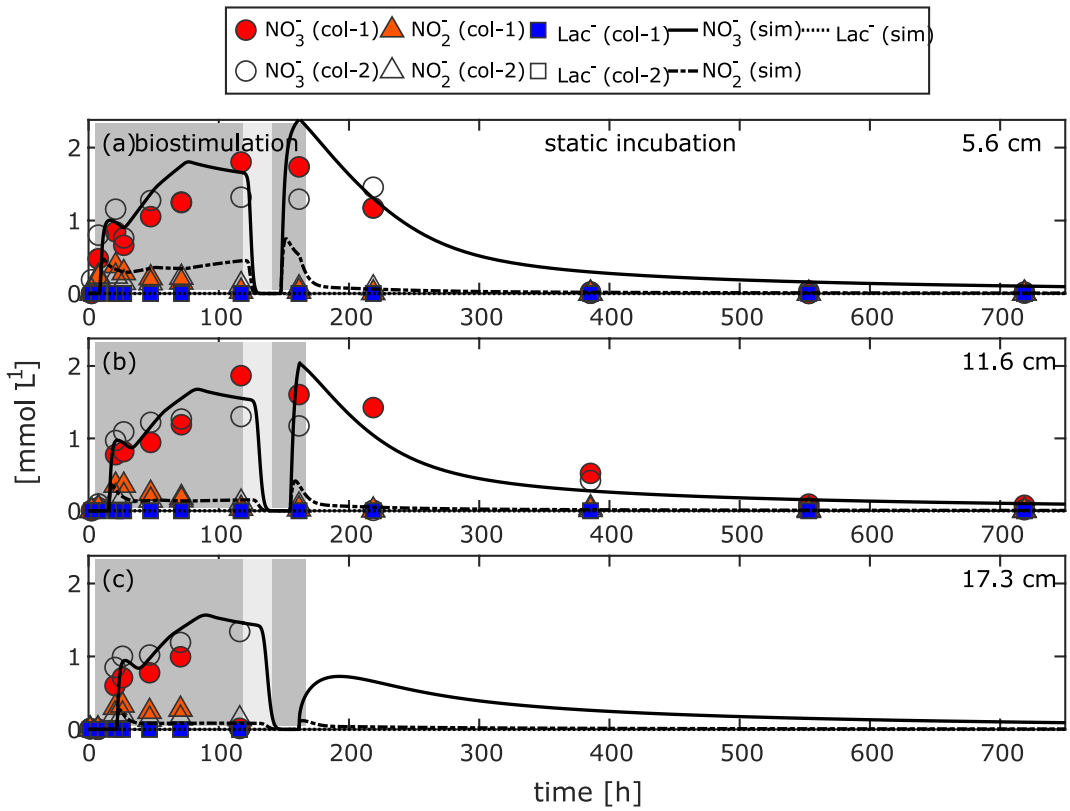

Figure 3. Concentration time series of NO_3^-, NO_2^- and lactate (Lac^-) during the biostimulation phase (gray background) and the static phase (white background) alongside the simulated concentrations at 5.6 cm (a), 11.6 cm (b) and at the outlet (c), $l = 17.3$ cm from the inlet. The light gray area separating the biostimulation phase denotes the 22 hr interruption in NO_3^- and lactate injection.

competitive sorption model sheds light on the geochemical variations that drive the SIP response in Tufa sediment during ion-exchange brought on by the injection of higher concentrations of monovalent ions and provides the basis for modeling bio-reactive transport during the biostimulation phase.

3.2. NO_3^--Biostimulation

In the following, we present the results of the biostimulation and the static incubation phases. During the preliminary biostimulation phases, neither NO_3^-, NO_2^- nor lactate was detected at any measurement location, indicating that denitrification took place in the first few cm at the column inlet. The corresponding concentration time series and SIP spectra of the preliminary flow phases are presented in Figures S11, S7e, S7f, S8, and S8f in Supporting Information S1. Geochemical data (i.e., major ions, pH and electrical conductivity) of the preliminary biostimulation phase and the main biostimulation phase are summarized in Figure S12 in Supporting Information S1.

3.2.1. Solute Concentrations

The biostimulation phase was initiated by an increase of the flowrate to 8.0 mL hr^{-1} (v: 0.18 m d^{-1}) and of the NO_3^--concentration to 2 mmol L^{-1}. It lasted for 162 hr and was followed by 840 hr of static incubation. Figure 3 presents measured and simulated breakthrough curves of NO_3^-, NO_2^-, and lactate at 5.6, 11.6 cm, and the outflow during both phases. NO_3^--breakthrough at 5.6 cm from the inlet was observed within 20 hr at around 50% of the inflow concentration, that is, 0.9 and 1.2 mmol L^{-1} in Col-1 and Col-2, respectively (Figure 3a). Concentrations of NO_3^- then increased up to 1.8 and 1.3 mmol L^{-1} at 117 hr NO_2^- accumulated up to 0.39 mmol L^{-1} 21 hr after the beginning of the biostimulation, followed by a decrease to less than 0.03 mmol L^{-1}.

During the biostimulation phase, aging of the tubing altered the ratio between the inflowing groundwater pumped via the peristaltic pump and the reactant-containing solution injected via the syringe pump. This resulted in a

constantly decreasing flow rate and a consequent increase in the injection concentrations of NO_3^- and lactate to 5 and 1.6 mmol L^{-1}, respectively. We accounted for this in our reactive transport model by implementing changing boundary conditions at the inflow (see Figure S13 in Supporting Information S1). The reactive transport model was fitted to the average concentrations of both columns. It captures the concentration breakthrough during denitrification quite well. After lactate was consumed within the uppermost centimeters close to the inlet, denitrification had to be coupled to the oxidation of organic material released from the sediment matrix. We found that an additional source of readily bioavailable organic carbon, yielding high denitrification rates only in the first centimeters, was required to predict the N-concentrations. Therefore, we implemented a lactate-dependent release of DOC as a result of enhanced hydrolysis of organic matter due to the priming with lactate (Blagodatskaya & Kuzyakov, 2008). From 119 to 142 hr (shown as a light gray background in Figure 3), the injection of NO_3^- and lactate stopped due to a technical problem. After this interruption, the biostimulation was resumed for another 20 hr until the pore water contained NO_3^- again.

The rise in NO_3^- upon re-injection was captured by the model at 11.6 cm, but slightly over-predicted at 5.6 cm. Similarly, during the static incubation (from 162 hr onwards in Figure 3), NO_3^- was consumed in less than 223 and 393 hr at 5.6 and 11.6 cm from the inlet, respectively, whereas the model predicts a more gradual decline, in particular, at 5.6 cm. The measured and modeled discrepancies suggest a more pronounced depth-distribution of denitrification activity in the columns than accounted for in our model. We attribute this to the additional influence of the continued priming effect of lactate at the inlet. Nevertheless, our model is able to predict differences in denitrification rates with depth and overall, captures the temporal dynamics of both columns throughout both incubation phases accurately. The mean model computed denitrification rates were 285 versus 200 μmol L^{-1} d^{-1} at 5.6 and 11.6 cm, respectively. The rates are 2–20 times higher than zeroth-order denitrification rates determined at different field sites without the presence of highly concentrated electron donors (Green et al., 2008; Tesoriero & Puckett, 2011) and on the order of field-derived denitrification rates in a riparian zone (Tesoriero & Puckett, 2011). Given the high content of organic carbon of 5.7% in this sediment, the resulting denitrification rates are reasonable and demonstrate that experimental conditions were close to natural field conditions.

3.2.2. SIP Response

Figure 4 presents a subset of the spectral signal changes in σ'', recorded during the biostimulation and static incubation phases in Col-1 at the 5.6 cm electrode pair, along with the temporal variations in the maximum σ'' (σ''_{max}) in Col-1 and Col-2 compared to the simulated fraction of active biomass. A more detailed summary of σ''-spectra measured in all columns is presented in Figures S7 and S8g–S8l in the Supporting Information S1.

The σ''-spectra in Figures 4a and 4b show that the charge storage in the Tufa pack increased during the biostimulation phase. These variations were most evident in the frequency range of 1–100 Hz. Compared to the spectra during the conservative-tracer injection (Figure 2f), the spectrum directly before the start of the (main) biostimulation phase (labeled $t = -1$ hr in Figure 4a) exhibited a different shape. The measured response developed a clear peak, with a maximum of 3.3 μS cm^{-1} at 3 Hz. In Col-1, the peak developed during the preliminary biostimulation phase (Figure S7d in Supporting Information S1), which already saw NO_3^- being injected, whereas in Col-2 the peak was absent in the preliminary phase (Figure S7e in Supporting Information S1) but appeared after ∼30 hr during the main biostimulation phase (Figure S7h in Supporting Information S1). Despite these subtle differences, the two replicates exhibited similar overall trends and polarization magnitudes.

The control column showed a minor increase in σ'' during the preliminary biostimulation phase of 0.9 μS cm^{-1} and then of 0.5 μS cm^{-1} during the main biostimulation phase reaching a peak value of 3.6 μS cm^{-1} at 100 hr (Figures S7f and S7i in Supporting Information S1). This increase was only observed at 5.6 cm, at 11.6 cm σ'' remained constant (Figures S8f and S8i in Supporting Information S1). Sulfate, present in the groundwater stock, was continuously injected into the columns at a concentration of ∼0.18 mmol L^{-1}. The increase of σ'' in the control coincided with a drop in sulfate concentrations (Figure S14 in Supporting Information S1). We speculate that it was used as an electron acceptor in the absence of nitrate (Miao et al., 2012), yielding the measured increase in SIP signals at 5.6 cm in the control column. This is also justified by the much less pronounced SIP-signals relative to the treated columns, in line with sulfate being a much lower energy-yielding electron acceptor.

The observed trends in the spectral responses translated to an increased σ''_{max} in both replicate columns (Figure 4c) of up to 2.4 μS cm^{-1} at 108 hr, reaching magnitudes of 5.4 and 5.9 μS cm^{-1} in Col-1 and Col-2, respectively (the corresponding phase shifts were 13.0 mrad in Col-1 and 12.3 mrad in Col-2, see Figure S9g and S9h in Supporting

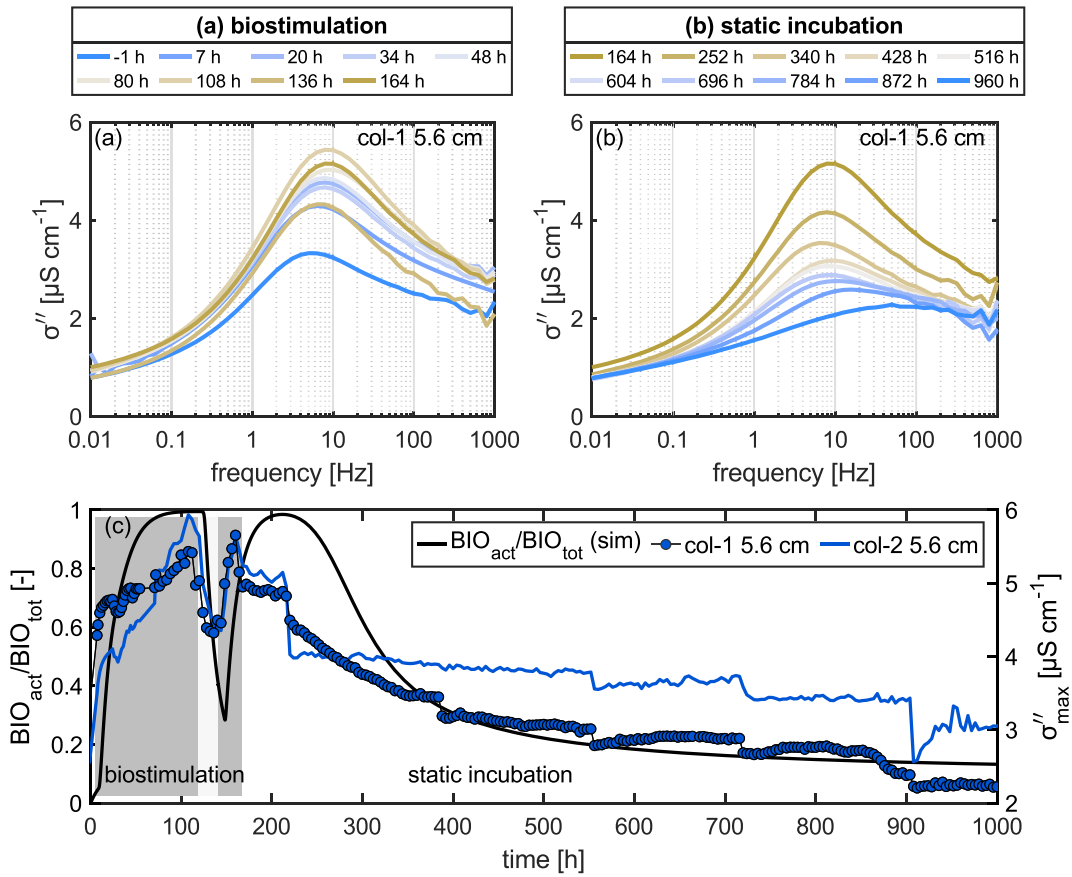

Figure 4. Selected spectra at 5.6 cm in Col-1 during (a) the biostimulation phase and (b) the static incubation phase. The fraction of simulated active biomass is compared to the maximum imaginary conductivity, σ''_{max}, at 5.6 cm in Col-1 and Col-2 in panel (c).

Information S1). Conversely, the real component of the complex conductivity, σ'_{max}, was approximately constant after the first 10 hr (e.g., 414.1 ± 24.2 µS cm^{-1} in Col-1) of the biostimulation phase (see Figure S15c in Supporting Information S1). The 22 hr period in which no NO_3^- was injected yielded a clearly visible drop in σ''_{max} of 1–1.6 µS cm^{-1}, followed by a recovery in the last 20 hr of the biostimulation phase. After stopping flow, which led to the gradual consumption of NO_3^- (Figure 3), σ'' decreased approximately exponentially by 1.9–2.9 µS cm^{-1} at all measurement locations until stabilizing after 500 hr. Once all NO_3^- was consumed the shape of the σ'' spectra shifted back to that measured during the abiotic tracer injection, that is, prior to biostimulation (Figure 4b). Thus, highlighting the full reversibility of the additional polarization contribution during microbial activity. Pore-water sampling caused drops in σ'' that were less evident during the biostimulation flow phase but resulted in irreversible stepwise changes during the static incubation. We speculate that these alterations were brought on by abrupt variations of the pore-water chemistry which were "washed out" in the presence of flow. During the static incubation phase σ' (see Figure S15d in Supporting Information S1), followed the trend of σ''. However, the relative decrease in σ' was less pronounced (−23% to −33%) than that of σ'' (−35% to −52%).

The frequency range of the peak σ'' during biostimulation observed herein agrees well with the frequency range reported for bacteria (Mellage, Holmes, et al., 2018; Mellage et al., 2019; Rosier et al., 2019; Zhang et al., 2014). Moreover, the reversibility of the distinct spectral characteristics after the bio-reactive phase point to a secondary, microbial contribution to our measured polarization responses. The agreement between the temporal trends in σ''_{max} and the simulated fraction of active biomass (Figure 4c), computed based on the fit of the reactive transport model to the geochemical breakthrough curves, provides further evidence to suggest that the unique spectral characteristics and changes in σ'' during biostimulation were brought on by the actively denitrifying microbial community in the Tufa sediment. However, the NaBr-injection showed that changes in pore-fluid conductivity and geochemical composition alter the Tufa's σ''. Therefore, to uniquely attribute changes in the magnitude of

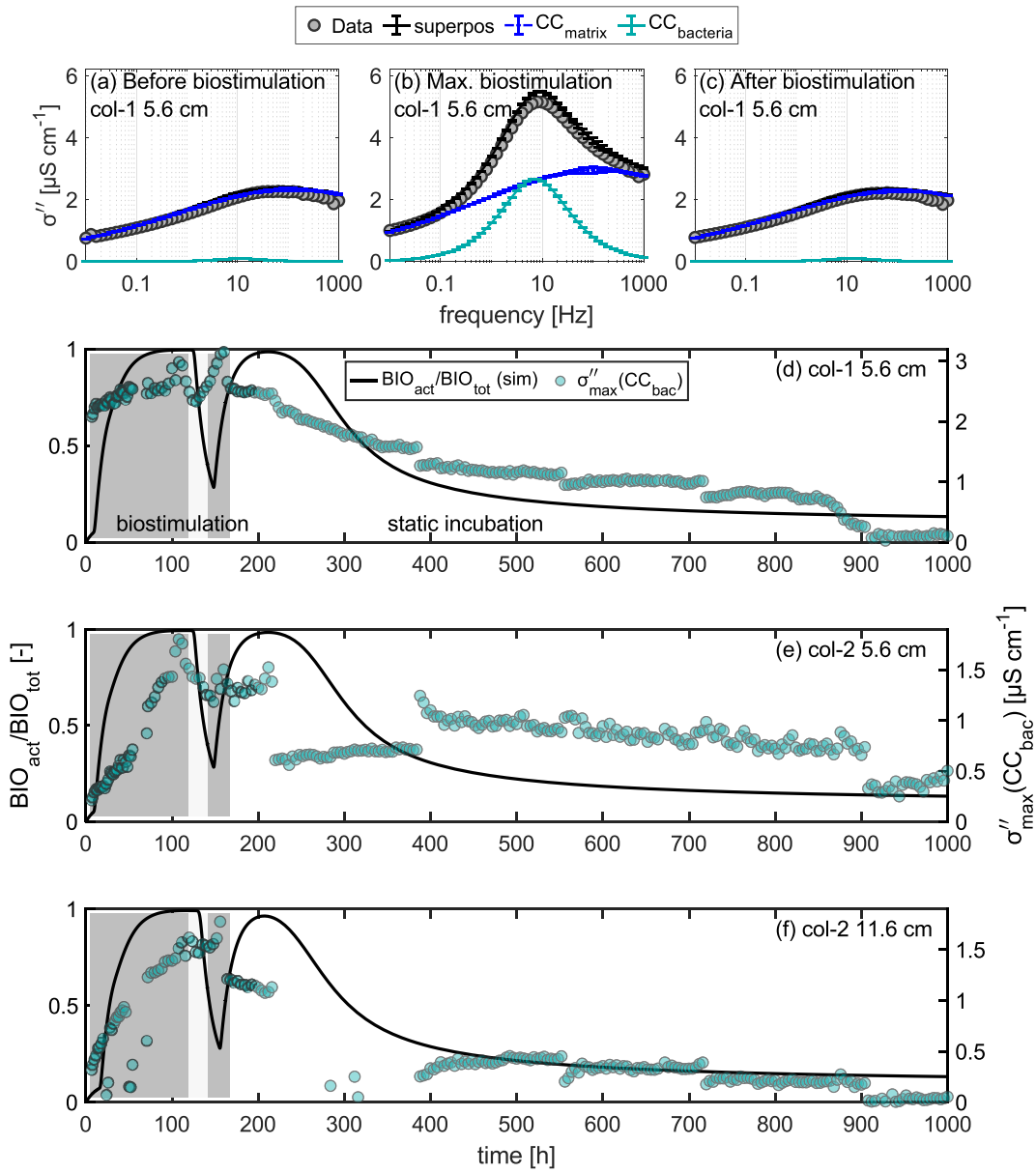

Figure 5. Cole-Cole decomposition of three example spectra recorded in Col-1 at 5.6 cm, before (a), at the peak of biostimulation (b) and after biostimulation (c), where CC_{matrix} and $CC_{bacteria}$ are the separate sediment and microbial contributions to the polarization signal. The simulated fraction of active biomass BIO_{act}/BIO_{tot} is compared to the σ''_{max} of the microbial Cole-Cole term during the biostimulation and the static incubation at 5.6 cm in Col-1 (d) and Col-2 (e) as well as at 11.6 cm in Col-2 (f).

σ''-maxima to microbial activity (Na^+ was injected as a counter ion during biostimulation), in the following, we separate parallel polarization contributions stemming from the EDL of the matrix and that of the microbes via a Cole-Cole decomposition.

3.2.3. Superimposed Polarization Mechanisms

In the following, we make use of the full spectral information to facilitate the direct interpretation of microbially-driven SIP responses. To this end, we apply a Cole-Cole decomposition approach to quantify the contribution of parallel polarization mechanisms to the overall SIP response.

Figure 5 shows the two-term Cole-Cole fit for three spectra, recorded before the first NO_3^--injection (Figure 5a), at the peak of biostimulation (Figure 5b) and at the end of the static incubation phase (Figure 5c). In all three

cases the superposition of matrix (Tufa sediment) and bacterial contributions adequately fit the behavior of the SIP data, with a slight overestimation during the phase of maximum denitrifying activity.

Before and after the biostimulation, the Cole-Cole decomposition attributed the polarization to the matrix component, CC_{matrix} only. As expected, charge storage during the NaBr-injection was solely attributed to CC_{matrix}, that is, no microbially-driven SIP signature was observed prior to biostimulation (Figures S16 and S18a–S18c in Supporting Information S1). During biostimulation, CC_{matrix} increased by approximately 0.5 μS cm^{-1}, which was expected due to the co-injection of Na^+ as the counter ion of NO_3^-, but a major part of the change compared to the pre-biostimulation spectra was attributed to $CC_{bacteria}$. At the peak frequency of the bacterial polarization, 6 Hz, the Cole-Cole decomposition predicted that matrix and bacteria contribute to a similar extent to the overall magnitude of charge storage. The latter highlights that the polarization of cell surfaces can play a significant role in natural sediments despite their small volume fraction.

After separating the bacterial polarization from the matrix polarization, we compare simulated microbial dynamics with the $\sigma''_{max}(CC_{bacteria})$ time series in Figures 5d–5f at 5.6 cm in Col-1 (d) and Col-2 (e) as well as at 11.6 cm in Col-2 (f). Indeed, there is a good match between $\sigma''_{max}(CC_{bacteria})$ and the model-predicted evolution of active biomass at the different SIP measurement locations during the biostimulation and, to lesser extent, in the static phase. The reactive transport model was fitted to the measured solute concentrations only, thus the good agreement in the trends between active biomass and $\sigma''_{max}(CC_{bacteria})$ provides a validation of our conceptual assumption that the polarization peak that we observed during the biostimulation was caused by microbial activity. While microbiological data, such as the quantification of functional genes and transcripts, could have further supported the relationship between σ'' and microbial activity, we chose to rely on concentration time series of duplicate columns rather than on an experimental setup that would allow sacrificial sampling for molecular-biological analyses. The unknown kinetics and long experimental run time would have required a series of ca. 10 columns per replicate (30 in total), making such an experiment unfeasible. Monod-type models based on concentration measurements have been shown to be equally good at predicting denitrification rates as gene-explicit models that incorporate molecular biological data (Störiko et al., 2021). We are, therefore, confident that our model yields an adequate representation the relative changes in microbial activity during our experiment.

Col-1 and Col-2 showed consistent temporal σ'' dynamics, but we also observed features that are not represented by the active biomass predicted by our reactive transport model. We attribute this to two main factors. First, the model does not account for the preliminary biostimulation phase and its effect on the level of microbial activity. The influence of antecedent biostimulation effects was particularly apparent in Col-1. Second, the pore water sampling exerted a strong effect on σ'' that caused marked offsets, especially at the beginning of the static incubation phase, particularly in Col-2.

Overall, the relative temporal dynamics of σ''_{max} ($CC_{bacteria}$) are similar to the measured σ''_{max} (Figure 4c) confirming that σ'' changes were dominated by microbial activity during denitrification. The most apparent difference between σ''_{max} and σ''_{max} ($CC_{bacteria}$) is the response to the 20 hr without the injection of NO_3^-. The decrease in $CC_{bacteria}$ by up to 0.6 μS cm^{-1} corresponds only to 26%–48% of the change in σ''_{max}. Thus, the Cole-Cole decomposition attributes a major part of the total decrease in σ''_{max} to the cation exchange on the matrix given that also Na^+ was not injected over the 20 hr period (Figure S20 in Supporting Information S1). This suggests that the effect on the activity of the microbial community is less strong, though still significant, than predicted by the reactive transport model or from interpreting the σ''_{max} data only. The removal of the simultaneously changing matrix polarization enables us to access the actual microbial polarization magnitudes, the relevant quantity for a future establishment of quantitative petrophysical relationships between σ'' and microbial abundance and activity in different sediments or for different reactions.

The response of $CC_{bacteria}$ to the absence of substrate is immediate, compared to the simulated active biomass. We speculate that the delayed response of the biomass activation is rather an artifact of the model and that the microbial response to NO_3^--concentration changes might be much faster. As already pointed out during the discussion of the model fit to the concentration measurements, the model underpredicts denitrification in the last 20 hr of biostimulation, suggesting that the time lag for responses of bacteria to changes in the nutrient supply may be significantly faster, such as the change in $\sigma''(CC_{bacteria})$, than currently predicted by the model.

The sensitivity of SIP to the activation of microbes may be explained by the microbes' ability to actively alter the structure of their cell wall and surrounding medium. During the energy metabolism of cells, an electrical potential between the extracellular matrix and the cytoplasm is formed by gradients of H^+ or Na^+ ions across the

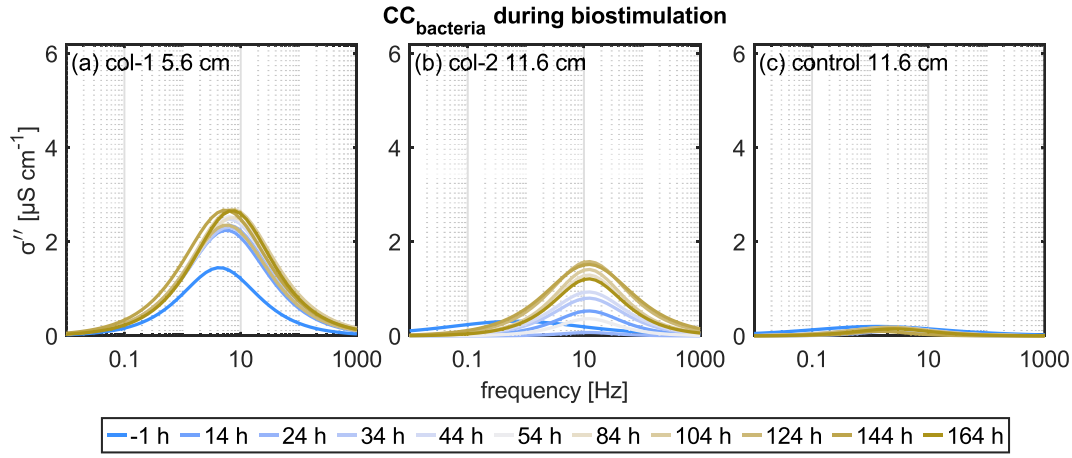

Figure 6. The Cole-Cole term that is associated with bacterial activity, $CC_{bacteria}$, is shown for specific timepoints during the main biostimulation phase in Col-1 at 5.6 cm (a), Col-2 at 11.6 cm (b) and in the control column at 11.6 cm (c).

cell membrane (Maloney et al., 1974). Bacteria can actively influence this gradient through their cell proteins (Konings et al., 2002) and are therefore also actively influencing the composition of the surrounding fluid. In addition, a large fraction of the cell membrane proteins, that can form up to 60% (w/w) of the cell membrane, are involved in solute transport processes, for example, using the H^+ or Na^+ gradients or ATP to actively transport substrates into or out of the cell (Konings et al., 2002). Since these active transport processes require energy, they depend on the activity of the microbes. The macroscopically observable polarization may thus not only be a function of the microbial abundance, but also the metabolic activity. Within the duration of our experiment, we did not expect significant changes in microbial abundance but definitely in their activity, as implemented in the reactive transport formulation. Consequently, we attribute the σ''-signal to changes in microbial activity. In particular, the immediate response of σ'' to the stop and restart of the NO_3^--injection points to a fast adaptation of the microbial community to changes in substrate concentrations rather than microbial decay and regrowth as the main influence on polarization. Thus far, this aspect has not been considered in the experimental design and interpretation of microbial SIP studies, but provides an explanation for the difference in polarization magnitude between studies that investigated microbial signals in the absence of reaction (and thus activity) (Abdel Aal et al., 2010; Zhang et al., 2014) to those in the presence of substrates (Joo et al., 2021; Mellage, Holmes, et al., 2018; Mellage et al., 2019; Rosier et al., 2019). In the absence of nutrients, reported σ'' changes are less than 1 µS cm^{-1}, whereas σ'' changes over several µS cm^{-1} have been observed in the presence of energy-yielding substrates, analogous to the signals recorded herein. We stress that at this state, the relative contributions of microbial abundance and activity as well as their effects on microbe polarization remain unknown, but that our work points toward a significant influence of metabolic activity on polarization that should be considered in future studies.

Figure 6 compares the $CC_{bacteria}$ spectra during the biostimulation phase between the top half of Col-1 (a), the bottom half of Col-2 (b), and the control column (c). Given that the columns were packed and treated in the same way (with the exception of the control not receiving NO_3^-), the results of the Cole-Cole decomposition should yield consistent results across all columns and the different measurement locations. Indeed, distinct differences, reflecting the intensity of bio-activity, are visible. Thus, the Cole-Cole decomposition of the SIP response may provide a means to quickly identify zones and times of high bio-activity independent of concentration data. The approach also enabled the identification of microbial activity in the upper half of the control column, related to sulfate reduction (Figure S14b in Supporting Information S1).

During the static incubation, the decomposition approach attributed the decrease in polarization to both the matrix (Figure S20 in Supporting Information S1) and the bacteria (Figures 5d–5f). In the static phase in general, the fitting was more challenging as the spectra started to show increasing noise at high frequencies likely due to aging of the electrodes toward the end of the experiment. Additionally, pore-water sampling altered the polarization of the matrix significantly and permanently under no-flow conditions, causing, for example, $CC_{bacteria}$ to be zero in Col-2 at 11.6 cm between two sampling events, at 215 and 384 hr (Figure 5f). Thus, we regard the Cole-Cole decomposition during the static phase to be strongly affected by data quality issues that hindered a robust parameter estimation and hence the interpretation of temporal dynamics is limited.

Cole-Cole model parameters have been shown to be highly correlated making parameter interpretation a challenge (Bérubé et al., 2017; Fiandaca et al., 2018). By reconverting the parameters into complex conductivity values, ambiguities in parameter estimation can be reduced because a subset of parameters is interpreted jointly. The high correlation between the parameters also causes challenges during parameter estimation. For the two-term Cole-Cole model it was therefore necessary to constrain the single parameters based on prior knowledge as described in Section 2.4. Nonetheless, the root-mean square error (RMSE) increased with an increase of $CC_{bacteria}$, ranging between 0.1 and 0.35 μS cm^{-1} during the main biostimulation phase (Figure S21a in Supporting Information S1). Model uncertainty estimates based on the covariance matrix of the parameters, derived via linear uncertainty propagation, yielded either unrealistically low (during the biostimulation phase, Figure S21b in Supporting Information S1) or extremely high uncertainties, in particular during the static incubation. For the demonstration of the separation of polarization processes within this work, the applied uncertainty analysis provided sufficient information on the reliability of the Cole-Cole decomposition during the different phases. For a future exploration of quantitative relationships between $CC_{bacteria}$ and microbiological data and models, a more rigorous posterior uncertainty quantification, for example by Markov-Chain Monte-Carlo methods, will be necessary.

4. Summary and Conclusions

This study has shown that SIP is sufficiently sensitive to microbial activity to enable monitoring of bio-reactive processes such as microbial denitrification under conditions that are comparable to those found at natural field sites, in terms of sediment and pore-fluid composition, reaction rates, and temperature. With heterotrophic denitrification, we chose a reactive process that does not involve precipitation or dissolution of polarizing minerals such that changes in charge storage could exclusively be attributed to changes in pore-water chemistry and/or microbial activity. In the biostimulation phase of our denitrification experiments, the observed changes in the SIP signal were dominated by microbial activity within the sediment columns, despite the presence of polarization processes by the background matrix. This conclusion is supported by multiple lines of evidence, namely, (a) a reactive transport model that captures the observed concentration time series and predicts maximum microbial activity at times of maximum increase in the imaginary conductivity magnitude, and (b) a decomposition of the complex-conductivity spectra that largely associates the increase in σ'' during biostimulation to a component that differs in its spectrum from that observed in the NaBr-injection phase, when the entire SIP-response was attributed to the change of pore-water chemistry.

We were successful at isolating the contribution of microbial processes from other parallel processes that might contribute to overall charge storage. The NaBr injection showed that alternative processes, for example, cation exchange can also cause an increase in σ''_{max} that might easily be misinterpreted. We propose an easy-to-implement Cole-Cole decomposition approach that helps to discriminate between parallel polarization contributions. The Cole-Cole decomposition successfully differentiated between microbially active and microbially inactive zones and times throughout our experiment. It allowed us to isolate the spectral contribution of a natural microbial community to σ'', facilitating the determination of the expected magnitude of microbially-driven polarization under varying conditions. Moreover, it can potentially provide information that is necessary for a quantitative comparison of different bio-reactive studies in natural sediments. We found an excellent agreement between the fraction of active biomass and the σ''_{max} determined by the Cole-Cole decomposition during biostimulation and the spectral responses recorded here agreed with σ''-spectra of single-strains in non-polarizing media (Mellage, Holmes, et al., 2018; Mellage et al., 2019; Rosier et al., 2019; Zhang et al., 2014). Further experiments that focus on the activation-deactivation pattern of microbes might reveal the potential of incorporating SIP data into reactive transport models for the quantitative estimation of microbial kinetic parameters such as the maximum specific growth rate constants and the activation/deactivation rate laws and coefficients.

Our Cole-Cole decomposition only requires the complex conductivity spectrum of the material prior to biostimulation and microbial conductivity spectra from other studies but no (site-specific) geochemical data are necessary to constrain the parameters. This opens new avenues for the application of SIP as a fast method to monitor a system's reactivity without the need to wait for geomicrobiological analysis. However, a rigorous uncertainty estimation and improved parameter optimization is required for improving the quantitative potential of the approach. In particular, Bayesian methods may be well suited to reliably assess the posterior parameter distribution. Finally, the approach would benefit, in future, from a detailed validation coupled to monitoring of microbiological markers including molecular-biological measurements of microbial activity.

Further development of the Cole-Cole decomposition approach may pave the way for the application of SIP as a real-time monitoring method in biogeochemical laboratory experiments. This is of particular value for reaction monitoring during experiments to inform the timing of geochemical sampling. In biotechnology studies, the potential of SIP as a process monitoring method is gaining increasing interest and has shown to have advantages in terms of transferability between different strains and conditions over traditional methods (Slouka et al., 2016, 2017; Turick et al., 2019).

With a frequency range of around 1–100 Hz, microbial polarization occurs within a range that is less prone to measurement errors of SIP (Dahlin et al., 2002; Pelton et al., 1978; Zimmermann et al., 2008), thus facilitating its potential for monitoring in the field. Enhanced in situ denitrification projects like that of Critchley et al. (2014) could benefit from SIP monitoring, providing information on the duration of the "conditioning" phase by detecting the onset of microbial activity from the SIP response. Multi-electrode SIP measurements and associated inversion may be used to locate microbial stimulation in the subsurface. For a better separation of microbial activity from other processes that influence complex conductivity in the subsurface, measurements over the entire frequency range, a spectral decomposition, a careful consideration of measurement errors, and further technological developments will be necessary.

Data Availability Statement

The SIP data, the geochemical data and the Matlab codes for the reactive transport modeling as well as the Cole-Cole fitting are available at https://doi.org/10.5281/zenodo.7032328 under the international Creative Commons license CC-BY-NC 4.0 (Strobel et al., 2022).

Acknowledgments
Adrian Mellage would like to acknowledge the financial support of the Baden-Württemberg Stiftung received for this project via the Eliteprogramme for Postdocs as well as the financial support of the Ministry for Science, Research and the Arts of Baden-Württemberg via the Research Seed Capital Program (RiSC). We thank Franziska Schädler, Verena Nickeleit and Monika Hertel (University Tübingen) for their support with chemical analysis, Aleksandra Pienkowska for support with qPCR measurements and Bernice Nisch for support with TOC measurements. The authors gratefully acknowledge the Tübingen Structural Microscopy Core Facility (Funded by the Federal Ministry of Education and Research (BMBF) and the Baden-Württemberg Ministry of Science as part of the Excellence Strategy of the German Federal and State Governments) for their support and assistance in this work, and the German Research Foundation DFG (INST 37/1027-1 FUGG) for financial support provided for the acquisition of the cryogenic focused ion beam scanning electron microscope. We thank Jeremiah Shuster and Stefan Fischer for their help with sample preparation and SEM imaging. Open Access funding enabled and organized by Projekt DEAL.

References

Abascal, E., Gómez-Coma, L., Ortiz, I., & Ortiz, A. (2022). Global diagnosis of nitrate pollution in groundwater and review of removal technologies. *Science of the Total Environment*, *810*, 152233. https://doi.org/10.1016/j.scitotenv.2021.152233

Abdel Aal, G. Z., Atekwana, E. A., Rossbach, S., & Werkema, D. D. (2010). Sensitivity of geoelectrical measurements to the presence of bacteria in porous media. *Journal of Geophysical Research*, *115*(G3), G03017. https://doi.org/10.1029/2009JG001279

Abdel Aal, G. Z., Atekwana, E. A., Slater, L. D., & Atekwana, E. A. (2004). Effects of microbial processes on electrolytic and interfacial electrical properties of unconsolidated sediments. *Geophysical Research Letters*, *31*(12), L12505. https://doi.org/10.1029/2004GL020030

Abdel Aal, G. Z., Slater, L. D., & Atekwana, E. A. (2006). Induced-polarization measurements on unconsolidated sediments from a site of active hydrocarbon biodegradation. *Geophysics*, *71*(2), H13–H24. https://doi.org/10.1190/1.2187760

Amrhein, C., & Suarez, D. L. (1990). Procedure for determining sodium-calcium selectivity in calcareous and gypsiferous soils. *Soil Science Society of America Journal*, *54*(4), 999–1007. https://doi.org/10.2136/sssaj1990.03615995005400040011x

Atekwana, E. A., & Slater, L. D. (2009). Biogeophysics: A new frontier in Earth science research. *Reviews of Geophysics*, *47*(4), L12505. https://doi.org/10.1029/2009RG000285

Ben Moshe, S., Kessouri, P., Erlich, D., & Furman, A. (2021). Geophysically based analysis of breakthrough curves and ion exchange processes in soil. *Hydrology and Earth System Sciences*, *25*(6), 3041–3052. https://doi.org/10.5194/hess-25-3041-2021

Bérubé, C. L., Chouteau, M., Shamsipour, P., Enkin, R. J., & Olivo, G. R. (2017). Bayesian inference of spectral induced polarization parameters for laboratory complex resistivity measurements of rocks and soils. *Computers and Geosciences*, *105*, 51–64. https://doi.org/10.1016/j.cageo.2017.05.001

Binley, A., & Slater, L. D. (2020). *Resistivity and induced polarization*. Cambridge University Press. https://doi.org/10.1017/9781108685955

Blagodatskaya, E., & Kuzyakov, Y. (2008). Mechanisms of real and apparent priming effects and their dependence on soil microbial biomass and community structure: Critical review. *Biology and Fertility of Soils*, *45*(2), 115–131. https://doi.org/10.1007/s00374-008-0334-y

Camargo, J. A., & Alonso, Á. (2006). Ecological and toxicological effects of inorganic nitrogen pollution in aquatic ecosystems: A global assessment. *Environment International*, *32*(6), 831–849. https://doi.org/10.1016/j.envint.2006.05.002

Che-Alota, V., Atekwana, E. A., Atekwana, E. A., Sauck, W. A., & Werkema, D. D. (2009). Temporal geophysical signatures from contaminant-mass remediation. *Geophysics*, *74*(4), B113–B123. https://doi.org/10.1190/1.3139769

Cole, K. S., & Cole, R. H. (1941). Dispersion and absorption in dielectrics I. Alternating current characteristics. *The Journal of Chemical Physics*, *9*(4), 341–351. https://doi.org/10.1063/1.1750906

Coleman, T. F., & Li, Y. (1996). An interior trust region approach for nonlinear minimization subject to bounds. *SIAM Journal on Optimization*, *6*(2), 418–445. https://doi.org/10.1137/0806023

Critchley, K., Rudolph, D. L., Devlin, J. F., & Schillig, P. C. (2014). Stimulating in situ denitrification in an aerobic, highly permeable municipal drinking water aquifer. *Journal of Contaminant Hydrology*, *171*, 66–80. https://doi.org/10.1016/j.jconhyd.2014.10.008

Dahlin, T., Leroux, V., & Nissen, J. (2002). Measuring techniques in induced polarisation imaging. *Journal of Applied Geophysics*, *50*(3), 279–298. https://doi.org/10.1016/S0926-9851(02)00148-9

Davis, C. A., Atekwana, E. A., Atekwana, E. A., Slater, L. D., Rossbach, S., & Mormile, M. R. (2006). Microbial growth and biofilm formation in geologic media is detected with complex conductivity measurements. *Geophysical Research Letters*, *33*(18), L18403. https://doi.org/10.1029/2006GL027312

Fiandaca, G., Madsen, L. M., & Maurya, P. K. (2018). Re-parameterisations of the Cole–Cole model for improved spectral inversion of induced polarization data. *Near Surface Geophysics*, *16*(4), 385–399. https://doi.org/10.3997/1873-0604.2017065

Gierczak, R. F. D., Devlin, J. F., & Rudolph, D. L. (2007). Field test of a cross-injection scheme for stimulating in situ denitrification near a municipal water supply well. *Journal of Contaminant Hydrology*, *89*(1–2), 48–70. https://doi.org/10.1016/j.jconhyd.2006.08.001

Green, C. T., Puckett, L. J., Böhlke, J. K., Bekins, B. A., Phillips, S. P., Kauffman, L. J., et al. (2008). Limited occurrence of denitrification in four shallow aquifers in agricultural areas of the United States. *Journal of Environmental Quality*, *37*(3), 994–1009. https://doi.org/10.2134/jeq2006.0419

Griebler, C., & Avramov, M. (2015). Groundwater ecosystem services: A review. *Freshwater Science*, *34*(1), 355–367. https://doi.org/10.1086/679903

Griebler, C., & Lueders, T. (2009). Microbial biodiversity in groundwater ecosystems. *Freshwater Biology*, *54*(4), 649–677. https://doi.org/10.1111/j.1365-2427.2008.02013.x

Groffman, P. M., Altabet, M. A., Böhlke, J. K., Butterbach-Bahl, K., David, M. B., Firestone, M. K., et al. (2006). Methods for measuring denitrification: Diverse approaches to a difficult problem. *Ecological Applications*, *16*(6), 2091–2122. https://doi.org/10.1890/1051-0761(2006)016[2091:MFMDDA]2.0.CO;2

Hao, N., Moysey, S. M. J., Powell, B. A., & Ntarlagiannis, D. (2015). Evaluation of surface sorption processes using spectral induced polarization and a (22)Na tracer. *Environmental Science & Technology*, *49*(16), 9866–9873. https://doi.org/10.1021/acs.est.5b01327

Joo, H.-W., Kwon, T.-H., Lee, S.-R., & Wu, Y. (2021). Relaxation behavior in low-frequency complex conductivity of sands caused by bacterial growth and biofilm formation by *Shewanella oneidensis* under a high-salinity condition. *Geophysics*, *86*(6), B389–B400. https://doi.org/10.1190/GEO2020-0213.1

Jougnot, D., Ghorbani, A., Revil, A., Leroy, P., & Cosenza, P. (2010). Spectral induced polarization of partially saturated clay-rocks: A mechanistic approach. *Geophysical Journal International*, *180*(1), 210–224. https://doi.org/10.1111/j.1365-246X.2009.04426.x

Katona, T., Gilfedder, B. S., Frei, S., Bücker, M., & Flores Orozco, A. (2021). High-resolution induced polarization imaging of biogeochemical carbon-turnover hot spots in a peatland. *Biogeosciences*, *18*(13), 4039–4058. https://doi.org/10.5194/bg-18-4039-2021

Kessouri, P., Furman, A., Huisman, J. A., Martin, T., Mellage, A., Ntarlagiannis, D., et al. (2019). Induced polarization applied to biogeophysics: Recent advances and future prospects. *Near Surface Geophysics*, *17*(6), 595–621. https://doi.org/10.1002/nsg.12072

Kimak, C., Ntarlagiannis, D., Slater, L. D., Atekwana, E. A., Beaver, C. L., Rossbach, S., et al. (2019). Geophysical monitoring of hydrocarbon biodegradation in highly conductive environments. *Journal of Geophysical Research: Biogeosciences*, *124*(2), 353–366. https://doi.org/10.1029/2018JG004561

Klingler, S., Cirpka, O. A., Werban, U., Leven, C., & Dietrich, P. (2020). Direct-push color logging images spatial heterogeneity of organic carbon in floodplain sediments. *Journal of Geophysical Research: Biogeosciences*, *125*(12), e2020JG005887. https://doi.org/10.1029/2020JG005887

Konings, W. N., Albers, S.-V., Koning, S., & Driessen, A. J. (2002). The cell membrane plays a crucial role in survival of bacteria and archaea in extreme environments. *Antonie van Leeuwenhoek*, *81*(1–4), 61–72. https://doi.org/10.1023/A:1020573408652

Kuypers, M. M. M., Marchant, H. K., & Kartal, B. (2018). The microbial nitrogen-cycling network. *Nature Reviews Microbiology*, *16*(5), 263–276. https://doi.org/10.1038/nrmicro.2018.9

Leckie, S. E., Prescott, C. E., Grayston, S. J., Neufeld, J. D., & Mohn, W. W. (2004). Comparison of chloroform fumigation-extraction, phospholipid fatty acid, and DNA methods to determine microbial biomass in forest humus. *Soil Biology and Biochemistry*, *36*(3), 529–532. https://doi.org/10.1016/j.soilbio.2003.10.014

Lennon, J. T., & Jones, S. E. (2011). Microbial seed banks: The ecological and evolutionary implications of dormancy. *Nature Reviews Microbiology*, *9*(2), 119–130. https://doi.org/10.1038/nrmicro2504

Leroy, P., & Revil, A. (2009). A mechanistic model for the spectral induced polarization of clay materials. *Journal of Geophysical Research*, *114*(B10), B10202. https://doi.org/10.1029/2008JB006114

Leroy, P., Revil, A., Kemna, A., Cosenza, P., & Ghorbani, A. (2008). Complex conductivity of water-saturated packs of glass beads. *Journal of Colloid and Interface Science*, *321*(1), 103–117. https://doi.org/10.1016/j.jcis.2007.12.031

Lesmes, D. P., & Morgan, F. D. (2001). Dielectric spectroscopy of sedimentary rocks. *Journal of Geophysical Research*, *106*(B7), 13329–13346. https://doi.org/10.1029/2000JB900402

Li, L., Sullivan, P. L., Benettin, P., Cirpka, O. A., Bishop, K., Brantley, S. L., et al. (2021). Toward catchment hydro-biogeochemical theories. *WIREs Water*, *8*(1), e1495. https://doi.org/10.1002/wat2.1495

Maloney, P. C., Kashket, E. R., & Wilson, T. H. (1974). A protonmotive force drives ATP synthesis in bacteria. *Proceedings of the National Academy of Sciences of the United States of America*, *71*(10), 3896–3900. https://doi.org/10.1073/pnas.71.10.3896

Marshall, D. J., & Madden, T. R. (1959). Induced polarization, a study of its causes. *Geophysics*, *24*(4), 790–816. https://doi.org/10.1190/1.1438659

Martin, S., Klingler, S., Dietrich, P., Leven, C., & Cirpka, O. A. (2020). Structural controls on the hydrogeological functioning of a floodplain. *Hydrogeology Journal*, *28*(8), 2675–2696. https://doi.org/10.1007/s10040-020-02225-8

Mellage, A., Eckert, D., Grösbacher, M., Inan, A. Z., Cirpka, O. A., & Griebler, C. (2015). Dynamics of suspended and attached aerobic toluene degraders in small-scale flow-through sediment systems under growth and starvation conditions. *Environmental Science & Technology*, *49*(12), 7161–7169. https://doi.org/10.1021/es5058538

Mellage, A., Holmes, A. B., Linley, S., Vallée, L., Rezanezhad, F., Thomson, N. R., et al. (2018). Sensing coated iron-oxide nanoparticles with spectral induced polarization (SIP): Experiments in natural sand packed flow-through columns. *Environmental Science & Technology*, *52*(24), 14256–14265. https://doi.org/10.1021/acs.est.8b03686

Mellage, A., Smeaton, C. M., Furman, A., Atekwana, E. A., Rezanezhad, F., & Van Cappellen, P. (2018). Linking spectral induced polarization (SIP) and subsurface microbial processes: Results from sand column incubation experiments. *Environmental Science & Technology*, *52*(4), 2081–2090. https://doi.org/10.1021/acs.est.7b04420

Mellage, A., Smeaton, C. M., Furman, A., Atekwana, E. A., Rezanezhad, F., & Van Cappellen, P. (2019). Bacterial stern layer diffusion: Experimental determination with spectral induced polarization and sensitivity to nitrite toxicity. *Near Surface Geophysics*, *17*(6), 623–635. https://doi.org/10.1002/nsg.12058

Mellage, A., Zakai, G., Efrati, B., Pagel, H., & Schwartz, N. (2022). Paraquat sorption- and organic matter-induced modifications of soil spectral induced polarization (SIP) signals. *Geophysical Journal International*, *229*(2), 1422–1433. https://doi.org/10.1093/gji/ggab531

Miao, Z., Brusseau, M. L., Carroll, K. C., Carreón-Diazconti, C., & Johnson, B. (2012). Sulfate reduction in groundwater: Characterization and applications for remediation. *Environmental Geochemistry and Health*, *34*(4), 539–550. https://doi.org/10.1007/s10653-011-9423-1

Morse, J. W., Arvidson, R. S., & Lüttge, A. (2007). Calcium carbonate formation and dissolution. *Chemical Reviews*, *107*(2), 342–381. https://doi.org/10.1021/cr050358j

Ntarlagiannis, D., Doherty, R., & Williams, K. H. (2010). Spectral induced polarization signatures of abiotic FeS precipitation. *Geophysics*, *75*(4), F127–F133. https://doi.org/10.1190/1.3467759

Ntarlagiannis, D., Williams, K. H., Slater, L. D., & Hubbard, S. S. (2005). Low-frequency electrical response to microbial induced sulfide precipitation. *Journal of Geophysical Research*, *110*(G2), G00G09. https://doi.org/10.1029/2005JG000024

Oldham, C. E., Farrow, D. E., & Peiffer, S. (2013). A generalized Damköhler number for classifying material processing in hydrological systems. *Hydrology and Earth System Sciences*, *17*(3), 1133–1148. https://doi.org/10.5194/hess-17-1133-2013

Pelton, W. H., Ward, S. H., Hallof, P. G., Sill, W. R., & Nelson, P. H. (1978). Mineral discrimination and removal of inductive coupling with multifrequency IP. *Geophysics*, *43*(3), 588–609. https://doi.org/10.1190/1.1440839

Pinay, G., Peiffer, S., de Dreuzy, J.-R., Krause, S., Hannah, D. M., Fleckenstein, J. H., et al. (2015). Upscaling nitrogen removal capacity from local hotspots to low stream orders' drainage basins. *Ecosystems*, *18*(6), 1101–1120. https://doi.org/10.1007/s10021-015-9878-5

Poonia, S. R., & Talibudeen, O. (1977). Sodium-calcium exchange equilibria in salt-affected and normal soils. *Journal of Soil Science*, *28*(2), 276–288. https://doi.org/10.1111/j.1365-2389.1977.tb02236.x

Poortinga, A. T., Bos, R., Norde, W., & Busscher, H. J. (2002). Electric double layer interactions in bacterial adhesion to surfaces. *Surface Science Reports*, *47*(1), 1–32. https://doi.org/10.1016/S0167-5729(02)00032-8

Rahman, W. A., & Rowell, D. L. (1979). The influence of magnesium in saline and sodic soils: A specific effect or a problem of cation exchange? *Journal of Soil Science*, *30*(3), 535–546. https://doi.org/10.1111/j.1365-2389.1979.tb01007.x

Revil, A., Atekwana, E. A., Zhang, C., Jardani, A., & Smith, S. (2012). A new model for the spectral induced polarization signature of bacterial growth in porous media. *Water Resources Research*, *48*(9), W09545. https://doi.org/10.1029/2012WR011965

Revil, A., & Florsch, N. (2010). Determination of permeability from spectral induced polarization in granular media. *Geophysical Journal International*, *181*(3), 1480–1498. https://doi.org/10.1111/j.1365-246X.2010.04573.x

Rezanezhad, F., Kleimeier, C., Milojevic, T., Liu, H., Weber, T. K. D., Van Cappellen, P., & Lennartz, B. (2017). The role of pore structure on nitrate reduction in peat soil: A physical characterization of pore distribution and solute transport. *Wetlands*, *37*(5), 951–960. https://doi.org/10.1007/s13157-017-0930-4

Rivett, M. O., Buss, S. R., Morgan, P., Smith, J. W. N., & Bemment, C. D. (2008). Nitrate attenuation in groundwater: A review of biogeochemical controlling processes. *Water Research*, *42*(16), 4215–4232. https://doi.org/10.1016/j.watres.2008.07.020

Rosier, C. L., Atekwana, E. A., Abdel Aal, G. Z., & Patrauchan, M. A. (2019). Cell concentrations and metabolites enhance the SIP response to biofilm matrix components. *Journal of Applied Geophysics*, *160*, 183–194. https://doi.org/10.1016/j.jappgeo.2018.10.023

Sanchis, A., Brown, A. P., Sancho, M., Martínez, G., Sebastián, J. L., Muñoz, S., & Miranda, J. M. (2007). Dielectric characterization of bacterial cells using dielectrophoresis. *Bioelectromagnetics*, *28*(5), 393–401. https://doi.org/10.1002/bem.20317

Saneiyan, S., Ntarlagiannis, D., & Colwell, F. (2020). Complex conductivity signatures of microbial induced calcite precipitation, field and laboratory scales. *Geophysical Journal International*, *224*(3), 1811–1824. https://doi.org/10.1093/gji/ggaa510

Saneiyan, S., Ntarlagiannis, D., Ohan, J., Lee, J., Colwell, F., & Burns, S. (2019). Induced polarization as a monitoring tool for in-situ microbial induced carbonate precipitation (MICP) processes. *Ecological Engineering*, *127*, 36–47. https://doi.org/10.1016/j.ecoleng.2018.11.010

Scheidegger, A. E. (1961). General theory of dispersion in porous media. *Journal of Geophysical Research*, *66*(10), 3273–3278. https://doi.org/10.1029/JZ066i010p03273

Schwarz, G. (1962). A theory of the low-frequency dielectric dispersion of colloidal particles in electrolyte solution 1,2. *The Journal of Physical Chemistry*, *66*(12), 2636–2642. https://doi.org/10.1021/j100818a067

Scott, J., & Barker, R. D. (2003). Determining pore-throat size in Permo-Triassic sandstones from low-frequency electrical spectroscopy. *Geophysical Research Letters*, *30*(9), 1450. https://doi.org/10.1029/2003GL016951

Shampine, L. F., & Reichelt, M. W. (1997). The MATLAB ODE suite. *SIAM Journal on Scientific Computing*, *18*(1), 1–22. https://doi.org/10.1137/S1064827594276424

Slater, L. D., & Glaser, D. R. (2003). Controls on induced polarization in sandy unconsolidated sediments and application to aquifer characterization. *Geophysics*, *68*(5), 1547–1558. https://doi.org/10.1190/1.1620628

Slouka, C., Brunauer, G., Kopp, J., Strahammer, M., Fricke, J., Fleig, J., & Herwig, C. (2017). Low-frequency electrochemical impedance spectroscopy as a monitoring tool for yeast growth in industrial brewing processes. *Chemosensors*, *5*(3), 24. https://doi.org/10.3390/chemosensors5030024

Slouka, C., Wurm, D. J., Brunauer, G., Welzl-Wachter, A., Spadiut, O., Fleig, J., & Herwig, C. (2016). A novel application for low frequency electrochemical impedance spectroscopy as an online process monitoring tool for viable cell concentrations. *Sensors*, *16*(11), 1900. https://doi.org/10.3390/s16111900

Stolpovsky, K., Martinez-Lavanchy, P., Heipieper, H. J., Van Cappellen, P., & Thullner, M. (2011). Incorporating dormancy in dynamic microbial community models. *Ecological Modelling*, *222*(17), 3092–3102. https://doi.org/10.1016/j.ecolmodel.2011.07.006

Störiko, A. (2019). Autosip (Version 1.0) (Computer software). Retrieved from https://github.com/astoeriko/autosip

Störiko, A., Pagel, H., Mellage, A., & Cirpka, O. A. (2021). Does it pay off to explicitly link functional gene expression to denitrification rates in reaction models? *Frontiers in Microbiology*, *12*, 684146. https://doi.org/10.3389/fmicb.2021.684146

Störiko, A., Pagel, H., Mellage, A., Van Cappellen, P., & Cirpka, O. A. (2022). Denitrification-driven transcription and enzyme production at the river-groundwater interface: Insights from reactive-transport modeling. *Water Resources Research*, *58*(8), e2021WR031584. https://doi.org/10.1029/2021wr031584

Strobel, C., Abramov, S., Huisman, J. A., Cirpka, O. A., & Mellage, A. (2022). Electronic appendix to: Spectral induced polarization (SIP) of denitrification-driven microbial activity in column experiments packed with calcareous aquifer sediments [Dataset]. Zenodo. https://doi.org/10.5281/zenodo.7032328

Tamir, G., Shenker, M., Heller, H., Bloom, P. R., Fine, P., & Bar-Tal, A. (2012). Dissolution and Re-crystallization processes of active calcium carbonate in soil developed on tufa. *Soil Science Society of America Journal*, *76*(5), 1606–1613. https://doi.org/10.2136/sssaj2012.0041

Tesoriero, A. J., & Puckett, L. J. (2011). O_2 reduction and denitrification rates in shallow aquifers. *Water Resources Research*, *47*(12), 12522. https://doi.org/10.1029/2011wr010471

Titov, K., Komarov, V., Tarasov, V., & Levitski, A. (2002). Theoretical and experimental study of time domain-induced polarization in water-saturated sands. *Journal of Applied Geophysics*, *50*(4), 417–433. https://doi.org/10.1016/S0926-9851(02)00168-4

Turick, C. E., Shimpalee, S., Satjaritanun, P., Weidner, J., & Greenway, S. (2019). Convenient non-invasive electrochemical techniques to monitor microbial processes: Current state and perspectives. *Applied Microbiology and Biotechnology*, *103*(20), 8327–8338. https://doi.org/10.1007/s00253-019-10091-y

van der Wal, A., Minor, M., Zehnder, A. J., & Lyklema, J. (1997). Conductivity and dielectric dispersion of gram-positive bacterial cells. *Journal of Colloid and Interface Science*, *186*(1), 71–79. https://doi.org/10.1006/jcis.1996.4615

Vaudelet, P., Revil, A., Schmutz, M., Franceschi, M., & Bégassat, P. (2011). Induced polarization signatures of cations exhibiting differential sorption behaviors in saturated sands. *Water Resources Research*, *47*(2), W02526. https://doi.org/10.1029/2010WR009310

Weller, A., & Slater, L. D. (2019). Permeability estimation from induced polarization: An evaluation of geophysical length scales using an effective hydraulic radius concept. *Near Surface Geophysics*, *17*(6), 581–594. https://doi.org/10.1002/nsg.12071

Werth, C. J., Zhang, C., Brusseau, M. L., Oostrom, M., & Baumann, T. (2010). A review of non-invasive imaging methods and applications in contaminant hydrogeology research. *Journal of Contaminant Hydrology*, *113*(1–4), 1–24. https://doi.org/10.1016/j.jconhyd.2010.01.001

Williams, K. H., Ntarlagiannis, D., Slater, L. D., Dohnalkova, A., Hubbard, S. S., & Banfield, J. F. (2005). Geophysical imaging of stimulated microbial biomineralization. *Environmental Science & Technology*, *39*(19), 7592–7600. https://doi.org/10.1021/es0504035

Zhang, C., Revil, A., Fujita, Y., Munakata-Marr, J., & Redden, G. (2014). Quadrature conductivity: A quantitative indicator of bacterial abundance in porous media. *Geophysics*, *79*(6), D363–D375. https://doi.org/10.1190/geo2014-0107.1

Zimmermann, E., Kemna, A., Berwix, J., Glaas, W., Münch, H. M., & Huisman, J. A. (2008). A high-accuracy impedance spectrometer for measuring sediments with low polarizability. *Measurement Science and Technology*, *19*(10), 105603. https://doi.org/10.1088/0957-0233/19/10/105603

References From the Supporting Information

Amalfitano, S., & Fazi, S. (2008). Recovery and quantification of bacterial cells associated with streambed sediments. *Journal of Microbiological Methods*, *75*(2), 237–243. https://doi.org/10.1016/j.mimet.2008.06.004

Griebler, C., Mindl, B., Slezak, D., & Geiger-Kaiser, M. (2002). Distribution patterns of attached and suspended bacteria in pristine and contaminated shallow aquifers studied with an in situ sediment exposure microcosm. *Aquatic Microbial Ecology*, *28*, 117–129. https://doi.org/10.3354/ame028117

Parkhurst, D. L. (1995). *Users guide to PHREEQC: A computer program for speciation, reaction-path, advective-transport, and inverse geochemical calculations*. U.S. Department of the Interior, U.S. Geological Survey, Earth Science Information Center, Open-File Reports Section (distributor). Retrieved from https://search.library.wisc.edu/catalog/999778194102121